



AMERICAN METEOROLOGICAL SOCIETY

Monthly Weather Review

EARLY ONLINE RELEASE

This is a preliminary PDF of the author-produced manuscript that has been peer-reviewed and accepted for publication. Since it is being posted so soon after acceptance, it has not yet been copyedited, formatted, or processed by AMS Publications. This preliminary version of the manuscript may be downloaded, distributed, and cited, but please be aware that there will be visual differences and possibly some content differences between this version and the final published version.

The DOI for this manuscript is doi: 10.1175/MWR-D-14-00163.1

The final published version of this manuscript will replace the preliminary version at the above DOI once it is available.

If you would like to cite this EOR in a separate work, please use the following full citation:

Penny, A., P. Harr, and M. Bell, 2015: Observations of a non-developing tropical disturbance in the western North Pacific during TCS-08 (2008). *Mon. Wea. Rev.* doi:10.1175/MWR-D-14-00163.1, in press.



Observations of a non-developing tropical disturbance in the western North Pacific during TCS-08 (2008)

Andrew B. Penny¹, Patrick A. Harr¹, and Michael M. Bell²

¹ Naval Postgraduate School, Monterey, California

² University of Hawai'i at Mānoa, Honolulu, Hawaii

PRELIMINARY ACCEPTED VERSION

¹ Corresponding author: Andrew B Penny, Naval Postgraduate School, Department of Meteorology, 589 Dyer Road, Root Hall, Room 254, Monterey CA 93943-5114, Email: abpenny@nps.edu

Abstract

2 Large uncertainty still remains in determining whether a tropical cloud cluster
3 will develop into a tropical cyclone. During THe Observing system Research and
4 Predictability Experiment (THORPEX) Pacific Asian Regional Campaign (T-PARC) /
5 Tropical Cyclone Structure-2008 (TCS-08) field experiment, over 50 tropical cloud
6 clusters were monitored for development, but only four developed into a tropical
7 cyclone. One non-developing tropical disturbance (TCS025) was closely observed for
8 potential formation during five aircraft research missions, which provided an
9 unprecedented set of observations pertaining to the large-scale and convective
10 environments of a non-developing system.

The TCS025 disturbance was comprised of episodic convection that occurred in relation to the diurnal cycle along the eastern extent of a broad low-level trough. The upper-level environment was dominated by two cyclonic cells in the tropical upper-tropospheric trough (TUTT) north of the low-level trough in which the TCS025 circulation was embedded. An in-depth examination of *in situ* observations revealed that the non-developing circulation was asymmetric and vertically misaligned, which led to larger system-relative flow on the mesoscale. Persistent environmental vertical wind shear and horizontal shearing deformation near the circulation kept the system from becoming better organized and appears to have allowed low equivalent potential temperature (θ_e) air originating from one of the TUTT cells to the north (up-shear) to impact the thermodynamic environment of TCS025. This in turn weakened subsequent convection that might otherwise have improved alignment and contributed to the transition of TCS025 to a tropical cyclone.

24 ***1. Introduction***

25 Only a small fraction of all tropical disturbances that occur over tropical ocean
26 basins develop into tropical cyclones (Gray 1982; Lee 1989; Simpson et al. 1997; Fu et
27 al. 2012). Gray (1998) commented that to adequately understand the process of tropical
28 cyclogenesis we must “thoroughly document the physical differences between those
29 systems which develop into tropical cyclones from those prominent tropical
30 disturbances which have a favorable climatological and synoptic environment, look
31 very much like they will develop but still do not.”

32 Radiosonde composites of developing and non-developing tropical systems in
33 the western North Pacific and North Atlantic were constructed by McBride (1981) and
34 McBride and Zehr (1981). The most notable characteristics differentiating the
35 developing composites were: (i) larger low-level relative vorticity; (ii) areas of nearly
36 zero vertical wind shear centered on the developing systems; and (iii) a vertical wind
37 shear structure in the surrounding environment indicative of an anticyclone aloft.

38 Analyses of more recent observations have led to several hypotheses regarding
39 tropical storm formation. Raymond and Sessions (2007), Raymond et al. (2011), and
40 Gjorgjevska and Raymond (2014) have suggested that a vertical mass flux maximum
41 in the low-levels, or a “bottom-heavy” mass flux profile, is most conducive for storm
42 formation through the horizontal flux convergence of low-level vorticity (i.e., low-level
43 spin-up), and that a stabilization of the thermodynamic profile results in lowering the
44 level of maximum vertical mass flux.

45 Davis and Ahijevych (2012, 2013) found evidence of this stabilization from
46 dropwindsonde data collected during the PRE-Depression Investigation of Cloud-

systems in the Tropics (PREDICT) field experiment (Montgomery et al. 2012), as low-level cooling occurred prior to storm formation for two developing systems. However, a similar study of PREDICT cases by Smith and Montgomery (2012) concluded that there was slight warming in the lower troposphere for both developing disturbances and the non-developing disturbance (Gaston) examined. Davis and Ahijevych (2012) suggested the low-level warming found by Smith and Montgomery (2012) could be due to the inclusion of dropwindsondes outside of the central convective region, which would act to obscure a lower-tropospheric cooling signal if present. Raymond and López Carrillo (2011) and Lussier et al. (2014) utilized high-resolution airborne Doppler radar and aircraft data to note that the level of maximum vertical mass flux lowered during the development of TY Nuri (2008), however the low-level mass flux calculated by Lussier et al. (2014) was stronger than that found by Raymond and López Carrillo (2011) earlier in the genesis process.

Differences in dropwindsonde moisture profiles for developing and non-developing systems during PREDICT were also examined. Komaromi (2013) found that non-developing systems were on average 10%-20% drier between 500 hPa and 700 hPa than the mean, but were actually more moist in the low levels. Komaromi (2013) suggested that mid-level dry air may have a larger negative impact on storm formation (through convective entrainment) compared to dry air in the low-levels. Davis and Ahijevych (2012) found that the mid-tropospheric moist static energy increased over time for the developing systems analyzed, while the non-developing system (Gaston) exhibited a decrease in moist static energy and an increase in downdraft convective available potential energy (DCAPE). Smith and Montgomery (2012) also found that the

70 mid- and upper-troposphere became progressively drier for Gaston and suggested that
71 the mid-level dry air observed in non-developing systems might act to dilute updraft
72 intensity and limit the amplification of lower-tropospheric vorticity by vortex stretching
73 (Bell and Montgomery 2010).

74 In addition to the thermodynamic and moisture considerations, the mesoscale
75 structure and vertical alignment of developing/non-developing circulations have also
76 been an area of recent focus. Davis and Ahijevych (2012) concluded that the vertical
77 misalignment of the vortex led to stronger system-relative flow for Gaston, which made
78 the incipient disturbance more susceptible to dry air in the surrounding environment.
79 Davis and Ahijevych (2012) suggested that continual deep convection might lead to
80 vortex realignment by initiating new lower-tropospheric circulations below the mid-
81 tropospheric circulation.

82 Raymond and López Carrillo (2011) found that vertically overlapping closed
83 circulations in the boundary layer and at 5-km elevation provided a deep region of
84 protection from negative environmental influences during the formation of TY Nuri.
85 Montgomery et al. (2010) suggested that despite the detrimental influences of strong
86 vertical wind shear and dry air during the early stages of TY Nuri, the presence of a
87 quasi-closed circulation in the system-relative frame (wave pouch) characterized by
88 recirculating flow (Dunkerton et al. 2009) protected the incipient vortex until it could
89 reach a more favorable environment. They further hypothesized that an increase in the
90 depth of the wave pouch is favorable for storm formation and may have occurred prior
91 to the formation of TY Nuri. Lussier et al. (2014) provided further evidence for the
92 importance of the wave pouch and its improved vertical alignment over time that

93 supported the mesoscale spin-up at low and mid-levels in TY Nuri. Similarly, Tory et
94 al. (2013) analyzed several cases of tropical storm formation in the Northern Australian
95 region and found that the vertical alignment of regions of recirculating, low-
96 deformation flow in the low- and mid-levels was important for further development.

97 During the combined T-PARC / TCS-08 field program in the western North
98 Pacific (Elsberry and Harr 2008), approximately 50 tropical cloud clusters were
99 identified in satellite imagery as potential precursors to tropical cyclone formation. Of
100 these, only 12 reached or exceeded tropical depression (TD) status. One of these non-
101 developing systems, referred to as TCS025, was closely monitored from 24 August
102 until 3 September 2008 since global models consistently predicted intensification (not
103 shown). However, development failed to occur. In this study, observations collected
104 during TCS025 (Fig. 1) are examined within the context of recent tropical cyclogenesis
105 theories to evaluate thermodynamic and dynamic factors associated with its non-
106 development. Since there often exists a great amount of uncertainty with respect to the
107 likelihood of formation (as was the case of TCS025), an in-depth analysis of a “null case”
108 is arguably just as important as documenting storm formation.

109 Based on an observational analysis, it will be shown that TCS025 was under the
110 influence of northerly vertical wind shear and within an environment characterized by
111 large horizontal shearing deformation. The circulation structure of TCS025 was vertically
112 misaligned such that system-relative flow (low- to mid-tropospheric vertical wind shear)
113 was larger compared to a vertically-aligned circulation. These factors combined to limit
114 organization, which allowed mid-level low equivalent potential temperature (θ_e) air to
115 impact the inner-core thermodynamic environment. This in turn weakened convection

116 and hindered further development. An outline for the remainder of this paper is as
117 follows: the data and methodology for this study are presented in section 2; section 3
118 details the synoptic and convective evolution of TCS025; a mesoscale analysis of the
119 aircraft-based *in situ* observations is contained in section 4; and a discussion of the
120 findings and conclusions are presented in section 5.

121

122 **2. Data and Methodology**

123 Aircraft missions during TCS025 were conducted by the United States Air Force
124 (USAF) 53rd Weather Reconnaissance Squadron (Hurricane Hunters) WC-130J and the
125 Naval Research Laboratory (NRL) P-3 over three intensive observing periods (IOPs)
126 (Fig. 1). Both aircraft collected flight-level data and the WC-130J retrieved surface wind
127 speeds and rain rates underneath the flight track using the onboard Stepped Frequency
128 Microwave Radiometer (SFMR) (Uhlhorn et al. 2007).

129 In total, 143 GPS dropwindsondes (Hock and Franklin 1999) were deployed
130 during the five aircraft missions into TCS025 and the surrounding environment (Fig. 1).
131 Dropwindsondes were deployed from about a 10-km altitude during the three WC-130J
132 missions. Since the P-3 was tasked to investigate convective features, its flight tracks
133 were far more irregular so dropwindsondes were deployed with variable spacing and
134 generally from below 3 km. All dropwindsonde data were quality controlled by the Earth
135 Observing Laboratory (EOL) at the National Center for Atmospheric Research (NCAR)
136 (Young et al. 2009a,b).

137 Dropwindsonde data were also used to analyze the vertical alignment of the
138 storm-relative circulation based on the method used by Davis and Ahijevych (2012). To

139 correct for sampling bias, Davis and Ahijevych (2012) first averaged the observations by
140 storm quadrant. However, due to the relatively weak and highly asymmetric wind
141 structure of TCS025, this procedure did not yield consistent results so all dropwindsonde
142 data were used in this study.

143 The ELectra DOppler RAdar (ELDORA) (Hildebrand et al. 1996; Wakimoto et
144 al. 1996), which was mounted on the tail of the P-3 during T-PARC/TCS-08 (Lee et al.
145 2009), allowed for an examination of the precipitation and circulation structure of the
146 non-developing TCS025 system over two consecutive days. Radial velocity data were
147 corrected for aircraft motion by using the method described in Testud et al. (1995). The
148 reflectivity and radial velocity fields underwent an additional quality control step to
149 remove radar artifacts, noise, ground clutter etc. using an automated procedure described
150 by Bell et al. (2013).

151 In addition to the observations collected during the IOPs, digital MTSAT IR
152 brightness temperatures at 0.05° -spatial and 30-minute-temporal resolutions were
153 azimuthally and radially averaged in cylindrical coordinates based on manually
154 determined center positions for TCS025. The cloud-top temperatures were used to infer
155 the average convective characteristics of the TCS025 environment. The MTSAT IR
156 brightness temperatures were also interpolated to the time and location of the
157 dropwindsondes to construct average dropwindsonde vertical profiles based on IR
158 brightness temperature values.

159 The European Center for Medium-Range Weather Forecasts (ECMWF) Year of
160 Tropical Convection (YOTC, Waliser et al. 2012) gridded analysis with $\sim 0.25^{\circ}$ horizontal
161 resolution at 6-h intervals was used to analyze the synoptic background and evolution of

162 TCS025. Earth-relative circulation center positions were identified from an examination
163 of 850 hPa ECMWF analysis streamlines for the time period encompassing aircraft
164 observations. When a closed circulation was not present, wind speed minima that
165 provided the best continuity with previous and future center positions were chosen. Later
166 in the evolution of TCS025, the earth-relative low-level circulation became disorganized
167 and displaced a considerable distance from the main area of low-level cyclonic relative
168 vorticity (see Fig. 2a). The 850 hPa vorticity maxima feature that was co-located with the
169 circulation center during IOP-2 was also tracked in time based on the ECMWF analysis
170 (see Fig. 2a). Since convection remained closer to the area of increased low-level
171 vorticity, the vorticity maxima positions were used to examine the temporal evolution of
172 vertical wind shear and IR brightness temperature.

173 The ECMWF analysis was also used to calculate the deep-layer (200-850 hPa)
174 and lower-tropospheric (500-850 hPa) environmental vertical wind shear by employing
175 the method of Davis et al. (2008). The irrotational and non-divergent components of the
176 vertical wind shear associated with the disturbance were removed from the total vertical
177 wind shear out to a radius of 450 km, and vertical wind shear was defined as the
178 difference between the resultant wind vectors at the center position. Since the TCS025
179 circulation remained relatively shallow and there were periods when it was not well
180 defined, the distinction between TCS025 and the surrounding environment was not
181 always clear. This may have impacted the environmental vertical wind shear calculations
182 during these periods.

183 To achieve as accurate an assessment of the true atmospheric state as possible,
184 data collected during the IOPs were combined with the ECMWF analysis using the

185 Spline Analysis at Mesoscale Utilizing Radar and Aircraft Instrumentation (SAMURAI)
186 analysis technique (Bell et al. 2012; Foerster et al. 2014), which provides a maximum
187 likelihood estimate of the atmospheric conditions through the minimization of a
188 variational cost function. Although dropwindsonde data were available for assimilation
189 into the ECMWF YOTC analysis fields, the flight-level and ELDORA dual-Doppler
190 radar data were not. SAMURAI analyses for IOP-2 and IOP-3 were conducted in the
191 storm-relative frame using two Cartesian analysis domains that: i) encompassed all
192 observations (5 km horizontal and 100 m vertical grid spacing), and ii) encompassed only
193 the ELDORA domain (2 km horizontal and 100 m vertical grid spacing). Due to the large
194 disparity between the typical spacing of ELDORA radial velocity observations and the
195 WC-130J dropwindsondes, the use of the ECMWF background field allowed for a 5 km
196 analysis without the need for excessive smoothing. Furthermore, comparisons with
197 additional analyses conducted without the use of a background field (not shown),
198 revealed minimal differences in the representation of the circulation structure. Additional
199 specifications for the SAMURAI analyses used in this study are given in Table 1 and in
200 Penny (2013, pp 46-47).

201

202 **3. System Evolution**

203 The TCS025 disturbance formed on the eastern periphery of a low-level trough
204 over the subtropical western North Pacific, and initially followed a track toward the
205 southeast before turning toward the north-northwest (Fig. 2a). Convection associated with
206 TCS025 was episodic and marked by development and decay of numerous mesoscale
207 convective systems (MCS) that occurred in the general region (Fig. 2) where TCS025

208 would later develop. Convective features associated with TCS025 that could be loosely
209 classified as MCSs were identified and tracked throughout its evolution. Convection
210 organized into a broad MCS (MCS-A) centered near 22°N, 152°E that reached peak
211 intensity measured by IR brightness temperature by 1130 UTC 25 August (Figs. 2 and 8).
212 This MCS moved quickly to the southeast, and by 0000 UTC 26 August only weak and
213 relatively disorganized convection remained. Deep convection continued to develop and
214 decay, and at 0645 UTC 26 August, MCS-D formed near 20°N, 150°E, which remained
215 the primary area of convection through the time of the first aircraft operation (Fig. 1).

216 At 0000 UTC 27 August (Fig. 3), the low-level trough extended from the
217 northwest to southeast and consisted of three circulations (Fig. 3c). Two tropical upper-
218 tropospheric trough (TUTT) cells (Fig. 3b) were in close proximity to the low-level
219 trough. At this time, the 200-850 hPa environmental vertical wind shear was northerly at
220 15 kt (Fig. 7). Upper-level diffluence between the TUTT cells to the north coincided with
221 the area of deep convection associated with MCS-D (Fig. 3a) that was near the central
222 low-level circulation (L2) at 22°N, 150°E (Fig. 3c). During the ensuing hours, MCS-D
223 fluctuated in intensity and structure and moved southward (Fig. 2a), presumably due to
224 the northerly flow aloft between the two TUTT cells (Fig. 3b). There was limited
225 convection along the eastern periphery of the low-level trough close to the low-level
226 circulation L3 (Fig. 3a). At 0845 UTC 27 August, MCS-D dissipated (see Fig. 2).

227 Over the next 24 h (Fig. 4), the low-level circulation L3 weakened and became
228 absorbed by L2 to the west (compare Figs. 3c and 4c). At this time, the eastern edge of
229 the low-level trough near 155°E was marked by strong confluence and southerly low-
230 level winds as L2 intensified (Fig. 4c). Convection (Fig. 4a) remained relatively

231 disorganized and weak until after 1200 UTC 27 August when the eastern-most TUTT cell
232 moved north-northeast of L2 (Figs. 4b,c). At 1045 UTC 27 August, MCS-G formed near
233 20°N, 150°E, which was close to the location where MCS-D had developed the day
234 before (Fig. 2). Similar to MCS-D, MCS-G moved southward before dissipating by 1145
235 UTC 28 August (Fig. 2). The MCS-G and its surrounding environment were the primary
236 foci of IOP-2. The environmental vertical wind shear magnitude was beginning to decline
237 at this time and reached a minimum of about 5 kt at 1200 UTC 28 August (see Fig. 7).

238 After the dissipation of MCS-G, convection remained disorganized and weak
239 until about 1800 UTC 28 August when MCS-H formed near 18°N, 154°E (Fig. 2), which
240 was in confluent flow east of L2. By 0000 UTC 29 August (Fig. 5), the eastern TUTT
241 cell weakened considerably (Fig. 5b) and was well northwest of L2 (Fig. 5c) and an
242 upper-level anticyclone was building above L2. Despite the development of an
243 anticyclone aloft, the environmental vertical wind shear began to increase (see Fig. 7) due
244 to the strengthening of the southerly flow along the eastern side of the low-level
245 circulation. An area of deep convection (Fig. 5a) was also present near a region of upper-
246 level diffluence east of the TUTT cell and extended farther east to the upper-level ridge
247 (MCS-I and MCS-J in Fig. 2). As TCS025 began to move northward following 1200
248 UTC 28 August, the earth-relative circulation center and vorticity maxima positions
249 began to separate considerably (see Fig. 2a), and the majority of the convection remained
250 near the vorticity maxima position, east of the low-level earth-relative circulation center.

251 By 0000 UTC 30 August (Fig. 6), the low-level circulation of TCS025 was no
252 longer closed in both the ground- and storm-relative frames and moved rapidly
253 northwestward as a low-level ridge strengthened to the south and east of TCS025 (Fig.

254 6c). Strong confluent southwesterly flow coincided with an area of increased convective
255 activity to the south-southeast of the L2 circulation. A cyclonically banded cloud
256 structure (Fig. 6a) became evident in MTSAT brightness temperature and a broad
257 anticyclone existed aloft (Fig. 6b).

258 Northerly 200-850 hPa vertical wind shear (Fig. 7a) continued to increase in
259 magnitude on 30 August as a result of the rapid northward translation of the system and
260 the impinging upper-level flow of another TUTT cell approaching from the east (not
261 shown). By 1200 UTC 30 August, convection that defined TCS025 became disorganized
262 and weak, and following 1800 UTC 30 August the cloud structure of TCS025 began to
263 dissipate (not shown). Between August 31 and September 1, the remnants of TCS025
264 underwent some extratropical development upon encountering a weak baroclinic zone to
265 the north (Davis et al. 2013).

266 Since the Raymond et al. (2011) study concluded that horizontal shear was an
267 important factor in the non-development of TCS025, the evolution of the average
268 normalized Okubo-Weiss (\mathcal{N}) parameter (Raymond et al. 2011) was examined (Fig. 7b).
269 The \mathcal{N} parameter allows for an assessment of the relative importance of the rotational
270 and deformational components of the horizontal flow. Values of \mathcal{N} range from -1 to +1.
271 Positive values indicate a larger rotational component of the flow and negative values
272 indicate that horizontal shear is large, which may prevent the consolidation of vorticity
273 and indicate the circulation of an incipient disturbance is less protected from the
274 detrimental effects of dry air in the surrounding environment (Raymond et al. 2011, Tory
275 et al. 2013). The evolution of average \mathcal{N} (Fig. 7b) indicates that the TCS025 environment
276 was dominated by large horizontal deformation throughout its evolution. As the vertical

277 wind shear magnitude decreased (Fig. 7a) following IOP-2, \mathcal{N} began to trend positive in
278 the low-levels, perhaps indicating that the system was experiencing some organization.
279 However, the increase in \mathcal{N} was brief and did not extend up to 500 hPa, which indicates
280 that the protective region of the pouch was quite shallow (Montgomery et al. 2010).

281 The convective intensity of the identified MCSs, defined as the brightness
282 temperature area $< -65^{\circ}\text{C}$ normalized by the brightness temperature area $< -35^{\circ}\text{C}$, varied
283 systematically with the diurnal cycle (Fig. 8). Convective intensity was highest around
284 1800 UTC daily, which approximately corresponds to the early morning oceanic
285 convective maximum time (Yang and Smith 2006; Park et al. 2011). The minimum in
286 convective intensity occurred shortly after 0000 UTC, which also corresponded to the
287 time that the majority of aircraft observations of TCS025 were collected (see Fig. 1).

288 To examine the average convective characteristics throughout the evolution of
289 TCS025, the IR brightness temperatures were radially averaged (Fig. 9) relative to the
290 850 hPa vorticity maxima positions. During the period when the vorticity maxima was
291 co-located with the low-level circulation center, the majority of convection formed south
292 of the center position, which was in the down-shear direction (Fig. 7a). Convection down
293 shear of the low-level center is consistent with previous studies that examined the tropical
294 cyclone convective response to vertical wind shear (Jones 1995; Frank and Ritchie 1999).
295 Although MCS-like features that formed near the convective maximum time (short
296 dashed lines in Fig. 9) were present at the time of each IOP, the radially averaged IR
297 brightness temperature indicates that convection was not as concentrated nor intense
298 leading up to IOP-3. In addition, the convective area remained small until well after 0000
299 UTC 29 August, which was later than the previous two days.

300

301 ***4. Mesoscale Analysis of In Situ Observations***

302 To examine the mesoscale structure of the TCS025 disturbance, the *in situ*
303 observations were examined and SAMURAI analyses were conducted for each IOP (Fig.
304 1) using dropwindsonde data, flight-level data, ELDORA dual-Doppler radar data (when
305 available), and the ECMWF YOTC analysis fields. Since the sampling coverage relative
306 to the circulation center was superior during IOP-2, data collected during this IOP will
307 receive the majority of attention in the analysis.

308

309 ***4.1 IOP-1 (1930 UTC 26 August – 0257 UTC 27 August)***

310 During IOP-1 centered at 0000 UTC 27 August, the WC-130J conducted a
311 “lawnmower” flight pattern (Fig. 10) and deployed dropwindsondes to sample the
312 environment of MCS-D (Fig. 3) that was beginning to decay while propagating
313 southward. Although earth-relative circulation center positions were determined as a
314 function of height from dropwindsonde data, uncertainties in the center positions were
315 too large to evaluate the vertical alignment of the circulation due to incomplete sampling
316 of the circulation. That said, the dropwindsonde center-finding method suggested two
317 low-level circulations (not shown) that agreed relatively well with the ECMWF analysis
318 (Fig. 3): the center providing the maximum average tangential wind near the surface
319 corresponded to circulation L2, whereas in the mid-levels it was closer to the location of
320 L3.

321

322 ***4.2 IOP-2 (2103 UTC August 27 – 0520 UTC 28 August)***

323 At the time of IOP-2, the low-level circulation was beginning a turn toward the
324 northeast (Fig. 2a). Because the first WC-130J aircraft mission had identified a
325 circulation center, the second mission was flown as a “square spiral” centered on the
326 estimated circulation center (Fig. 11). Similar to the previous day, a large MCS (MCS-G)
327 was present south of the circulation center (Fig. 11).

328 An examination of the dropwindsonde winds from IOP-2 reveals that the
329 circulation of TCS025 was highly asymmetric (Fig. 12). The strongest low-level winds
330 were westerly and southwesterly in the south and southeast portions of the WC-130J
331 flight domain. Over the western portion of the domain, the low-level circulation was
332 relatively weak. The strongest mid-level winds were northerly and northwesterly on the
333 western side of the mid-level circulation near 18.5°N, 151°E (Fig. 12).

334 Dropwindsonde coverage (Figs. 11 and 12) relative to the circulation center was
335 much more evenly distributed than during IOP-1 or IOP-3. The dropwindsonde-based
336 center analysis in the storm-relative frame reveals that the circulation centers were poorly
337 aligned in the vertical. The low-level circulation tilted toward the east with height, while
338 above 2 km the circulation tilted toward the southeast (Fig. 12).

339 Storm-relative circulation center positions were also identified as a function of
340 height using streamlines from the SAMURAI analysis (Fig. 12), which included
341 ELDORA Doppler radar data. The SAMURAI analysis revealed a fractured circulation
342 structure in the vertical; the low-level circulation was located near 19.5°N, 152.5°E and
343 only extended to 2-km height, and the circulation centers between 2.5- and 6-km height
344 were a considerable distance south-southwest of the low-level circulation.

345 The differences in center positions between the dropwindsonde method and the
346 SAMURAI analysis (Fig. 12) may be partly a result of not correcting for the sampling
347 bias in dropwindsonde coverage (see Section 2). However, additional tests revealed little
348 difference in the dropwindsonde-derived center positions when P-3 dropwindsondes were
349 excluded from the calculation (not shown), suggesting the impact from sampling bias was
350 minimal for this case. Instead, contrasts in horizontal resolution may have contributed to
351 the differences in circulation center positions. Whereas dropwindsondes were generally
352 deployed with 100-km spacing, the SAMURAI analysis had 5-km grid spacing. Thus, the
353 scales of motion sampled by the dropwindsondes were most likely larger than that
354 resolved by the SAMURAI analysis, especially over the area impacted by the ELDORA
355 radar winds. Nevertheless, both sources identify a low-level center that is displaced north
356 of a mid-level center.

357 The SAMURAI analysis for IOP-2 also reveals an asymmetric vortex structure in
358 the low- and mid-levels (Fig. 13). The circulation in the mid-troposphere was stronger
359 than the low-level circulation, which is indicative of a cold-core circulation. At this time,
360 the mid-level circulation center (red dot in Fig. 13) was positioned ~110 km to the south-
361 southwest of the low-level circulation center (black dot in Fig. 13). Low- to mid-
362 tropospheric vertical wind shear resulted from the relative locations of the mid- and low-
363 level circulations; northeasterly flow near 19°N, 151.2°E in the northwest quadrant of the
364 mid-level circulation (Fig. 13a) was positioned nearly above the center of the low-level
365 circulation.

366 The potential impact of the vertical misalignment was examined by comparing the
367 average mesoscale vertical wind shear (system-relative flow) in the storm-relative

368 SAMURAI analysis between 5- and 1.5-km height (Fig. 13) with an identical pseudo-
369 aligned circulation (i.e., as if the mid- and low-level circulations were vertically aligned).
370 The system-relative flow for the misaligned circulation was computed as the difference
371 between the 5- and 1.5-km box average wind vectors centered over the 1.5-km circulation
372 (dashed black box - solid black box in Fig. 13), whereas the pseudo-aligned system-
373 relative flow was defined as the difference between the 5- and 1.5-km box average wind
374 vectors centered on their respective circulation centers (solid red box - solid black box in
375 Fig. 13). The system-relative flow for the misaligned circulation was 9.3 kt from the
376 northeast (see Fig. 7a), whereas the system-relative flow for the pseudo-aligned
377 circulation was only 5.4 kt from the north-northwest. This indicates that the misalignment
378 of the circulation resulted in a larger system-relative flow than if the circulation had been
379 vertically aligned. The environmental 500-850 hPa vertical wind shear was very similar
380 in magnitude and direction to the pseudo-aligned case during this time (Fig. 7a), which
381 illustrates that the low-level vertical wind shear experienced locally by the system (on the
382 mesoscale) due to misalignment can be considerably different from the computed
383 environmental vertical wind shear.

384 To analyze the impact of including the ELDORA radial velocity observations in
385 the SAMURAI analysis, south to north vertical cross sections through the mid- and low-
386 level circulation centers of the ECMWF analysis background field (Fig. 14a) and the
387 SAMURAI analysis (Fig. 14b) were compared. The ECMWF analysis (Fig. 14a)
388 possessed a much stronger low-level circulation that tilted southward into the mid-
389 troposphere. In contrast, the SAMURAI analysis (Fig. 14b) depicted a strong mid-level
390 circulation near 6-km height that was almost entirely separate from a shallow and much

391 weaker low-level circulation to the north. The low-level wind field of the SAMURAI
392 analysis more closely resembled the broad trough observed the day before (see Fig. 3c)
393 rather than the well-defined low-level circulation of the ECMWF analysis. The low-level
394 circulation in the SAMURAI analysis was outside the range of the ELDORA Doppler
395 radar (black lines below the abscissa in Fig. 14b), so the vorticity magnitude was
396 primarily determined by the dropsondes in that region. The lack of radar data results in a
397 higher uncertainty in the vorticity magnitude, but the analysis suggests that the low-level
398 circulation is weaker than that in the ECMWF analysis.

399 The divergence profile near the low-level vorticity feature in the SAMURAI
400 analysis (Fig. 14b) appears to be a result of Ekman pumping, with frictionally-induced
401 convergence within the boundary layer and divergence immediately above the boundary
402 layer. Mid-level convergence was co-located with the mid-level vorticity feature to the
403 south, typical of a mesoscale convective vortex (MCV) (Raymond and Jiang 1990;
404 Bartels and Maddox 1991; Houze 2004). In addition, there was a positive temperature
405 anomaly in the SAMURAI analysis above 6.5 km height over a negative low-level
406 temperature anomaly (not shown), which is also characteristic of the thermal structure of
407 a balanced mid-level vortex (Chen and Frank 1993). Winds in the plane of the cross
408 section were northerly with some positive vertical motion extending from an area of mid-
409 tropospheric low- θ_e air associated with the TUTT toward the mid-level vorticity feature,
410 and low-level southerlies were present south of the mid-level vorticity feature.

411 Based on the SAMURAI (ELDORA) divergence profile (Fig. 14b) and the
412 ELDORA reflectivity pattern at 5-km height (Fig. 15), the region surrounding the mid-
413 level circulation had large areas of stratiform precipitation during IOP-2. Stratiform

414 precipitation processes likely contributed to the strengthening and maintenance of the
415 midlevel vortex at the expense of low-level spin-up. As argued by Tory et al. (2006), the
416 divergence profile associated with stratiform precipitation (low-level divergence and
417 mid-level convergence) would be detrimental to the spin-up of the low-level circulation.

418 A south-to-north vertical cross section of θ_e constructed from dropwindsonde data
419 (Fig. 16) west of the midlevel circulation center during IOP-2 (and west of the cross
420 section in Fig. 14) reveals lower values of θ_e near the surface in the dropwindsonde
421 profiles deployed at 0338, 0046, 0324, and 0231 UTC (Fig. 16). As indicated in Fig. 11,
422 the WC-130J was passing through the southern region of MCS-G at the time of the 0046
423 UTC dropwindsonde. The SFMR rain rates (Fig. 17, blue line) corresponding to the time
424 of the 0046 UTC dropwindsonde confirm the presence of precipitation, and MTSAT IR
425 brightness temperature, which was interpolated spatially and temporally to the WC-130J
426 flight track (Fig. 17, red line), reveals low cloud-top temperatures indicative of a
427 convective environment. Therefore, these regions of low-level low- θ_e air are interpreted
428 as resulting from convective downdrafts. Above the near-surface cold pool in the 0046
429 UTC profile (Fig. 16), a plume of increased θ_e relative to the background environment
430 extended into the upper levels, which is an indication of deep moist convection. By
431 contrast, an extensive region of low- θ_e air in the mid-troposphere north of the convective
432 region (up-shear) is also evident in Fig. 16, which was relatively cold, dry air associated
433 with the TUTT cell to the north (near 24°N, 154°E in Fig. 4b).

434

435 **4.3 IOP-3 (2234 UTC 28 August – 0510 UTC 29 August)**

436 At the time of IOP-3, the translation of the low-level circulation had increased
437 significantly toward the north-northwest (see Fig. 2a) and the wind structure was highly
438 asymmetric due to the increasing low-level pressure gradient along the eastern side of the
439 circulation (Fig. 5c). The third IOP was designed based on the broad cyclonically banded
440 convective structure of MCS-H, which was almost entirely south of the circulation center
441 in both the storm- and earth relative frames (Fig. 18). This resulted in observations being
442 south-southeastward of the circulation center. Because the P-3 flight track was designed
443 to circumnavigate the disturbance, the ELDORA radar coverage was limited to a narrow
444 swath around the periphery of the disturbance, which did not allow for a detailed analysis
445 of the convective structure or the winds near the circulation center to the north.

446 Despite these data coverage limitations, the SAMURAI analysis in the ground-
447 relative frame (not shown) and the 1.5 km dropwindsonde winds in Fig. 18a indicated
448 strong southerlies along the east side of the low-level circulation with almost no northerly
449 return flow on the western side of the circulation due to the rapid translation speed of the
450 system. A diagnosis of the circulation structure from the storm-relative SAMURAI
451 analysis (Fig. 18b) indicated that the low-level circulation on the northern periphery of
452 the flight domain was elongated and shallow, as it only extended from the surface to 2-
453 km height. Furthermore, the mid-level circulation was displaced to the south (not shown),
454 which was similar to the vertical structure observed during IOP-2.

455

456 **4.4 Thermodynamic evolution**

457 For each of the three WC-130J flights, MTSAT IR brightness temperatures were
458 interpolated to the location and time of each dropwindsonde. Average vertical profiles of

459 relative humidity, θ_e , and DCAPE were created for each flight for all dropwindsondes
460 with corresponding IR brightness temperatures less than -35°C and for those with an IR
461 brightness temperature greater than -35°C, which allowed for a comparison of the
462 thermodynamic conditions of the convective and non-convective environments,
463 respectively.

464 The average profiles reveal low-level relative humidity (Fig. 19a) was quite high
465 ($> 80\%$) throughout all IOPs in both the convective and non-convective environments.
466 However, mid- and upper-level relative humidity in the non-convective environment
467 decreased during IOP-2 (0325W) before increasing during IOP-3 (0525W). Similar
468 trends existed in the mid- and upper-tropospheric θ_e (Fig. 19b). Low- θ_e air observed
469 during IOP-2 resulted from the TUTT cell to the north being in close proximity to
470 TCS025 (see Figs. 4b and 16). The largest values of DCAPE in the non-convective
471 environment also existed during IOP-2 (Fig. 19c). Therefore a potential for strong
472 downdrafts existed if dry environmental air associated with the TUTT mixed into the
473 convective environment. By IOP-3, the TUTT cell had weakened considerably and had
474 moved a significant distance away from TCS025 (see Fig. 5b), which lessened its
475 thermodynamic impact on TCS025. In addition, the mid-level circulation (and region of
476 higher- θ_e air) became increasingly elongated in the north-south direction leading up to
477 IOP-3 (see Fig. 20f). Low- θ_e air was still present to the west and southeast of the mid-
478 level circulation, but the flight tracks of the WC-130J and P-3 remained almost
479 exclusively within this higher- θ_e air (not shown), which may partially account for the
480 rebound in thermodynamic conditions observed during IOP-3.

481 Profiles of average temperature anomalies (Fig. 19d) from dropwindsondes
482 deployed within 250 km of the circulation center reveal that the lower-tropospheric near-
483 surface layer was ~0.5 K colder relative to the dropwindsonde mean, and the middle and
484 upper levels were generally warmer. During IOP-2 (missions 0225W and 0325W), the
485 inner-core environment was colder than during IOP-1 or IOP-3. Similar to the relative
486 humidity, θ_e , and DCAPE profiles, this is believed to have been due to the
487 thermodynamic influence of the TUTT cell to the north.

488 The evolution of mid-level θ_e based on the ECMWF analysis prior to and
489 extending past IOP-2 reveals low- θ_e air to the north of the broad mid-level circulation at
490 1200 UTC 27 August (Fig. 20a). The lowest θ_e air was near 23.5°N, 156°E and a
491 trajectory analysis (not shown) reveals it was associated with the upper-level TUTT cell.
492 By 0000 UTC 28 August (Fig. 20c), low- θ_e air had moved westward to become
493 positioned north of the strengthening mid-level circulation. The low- θ_e air was being
494 advected southward along the western side of the mid-level circulation (Figs. 20c-e). By
495 1200 UTC 28 August (Fig. 20e), low- θ_e air (~335 K) had reached 18°N near 151°E while
496 the lowest θ_e air associated with the TUTT cell continued to move farther to the
497 northwest (Fig. 20f). Although the system-relative winds at 500 hPa (Fig. 20) do not
498 clearly indicate a direct pathway for low- θ_e air to enter the inner core of TCS025, the
499 negative normalized Okubo-Weiss values in the low- and mid-levels (Fig. 7b) indicates
500 there was large horizontal shearing deformation surrounding the circulation, and suggests
501 TCS025 lacked a quasi-closed circulation (see Tory et al. 2013). As a result, the
502 circulation was more susceptible to the entrainment of low- θ_e air to the west of the
503 circulation following 0600 UTC 28 August (Figs. 20d,e,f), and to the southeast of the

504 circulation following 1200 UTC 28 August (Figs. 20e,f). The presence of low- θ_e air in
505 the inner core is also suggested by the large negative low-level temperature anomalies
506 observed from average dropwindsonde profiles of the inner-core environment during
507 IOP-2 (Fig. 19d).

508 Near the end of IOP-2, deep convection associated with MCS-G was beginning to
509 weaken, which is indicated by the broad areas of weak reflectivity in Fig. 15. This time
510 corresponded to the waning stages of the diurnal convective cycle (see dashed lines in
511 Fig. 9). Although convection was present during the third IOP on 29 August, it appeared
512 less organized than during the second IOP, and less intense based on average IR
513 brightness temperatures (Fig. 9). In fact, there was a notable decline in convection after
514 0000 UTC 28 August in this region, and convection did not organize until the system had
515 moved a considerable distance north (see Fig. 6a). This suggests that the low- θ_e air
516 associated with the TUTT to the north of TCS025 led to a reduction in deep convection
517 after this time.

518

519 **5. Discussion and Conclusions**

520 The large-scale conditions conducive to tropical storm formation have been
521 known for some time: high SST ($>26.5^{\circ}\text{C}$), abundant low- and mid-level moisture,
522 convective instability, small vertical wind shear, and increased low-level relative vorticity
523 (Gray 1975). In general, these conditions were present for TCS025; SSTs were greater
524 than 29°C (not shown), and although the vertical wind shear magnitude was considerable
525 at times (~ 15 kt), there were periods when it was much lower. Therefore, a careful
526 examination of the mesoscale structure and interactions with the surrounding

527 environment is necessary to explain possible reasons for the non-development of
528 TCS025.

529 Vertical misalignment of the circulation caused the low- to mid-tropospheric
530 vertical wind shear (system-relative flow) to be larger in magnitude relative to a well-
531 aligned circulation. Based on IR brightness temperatures, convection was relatively weak
532 for TCS025, especially considering that the coldest cloud tops are generally found in the
533 western North Pacific (Liu et al. 2007). Deep convection that did form developed away
534 from the circulation and tended to move southward (i.e., down shear) away from the low-
535 level circulation. Given the appreciable misalignment of the circulation and the relatively
536 weak and asymmetric tangential wind field, it appears that the convective activity
537 associated with TCS025 was insufficient to promote vortex alignment as proposed by
538 Davis and Ahijevych (2012), or further development while in the presence of negative
539 environmental influences (i.e., vertical wind shear and low- θ_e air). Horizontal shearing
540 deformation was also quite large in magnitude throughout the evolution of TCS025, and
541 Raymond et al. (2011) concluded that it was an important factor in the non-development
542 of TCS025. This likely prevented further organization of convection and kept vorticity
543 from consolidating. Large horizontal flow deformation in the low- and mid-troposphere
544 indicates a deep recirculation region was not present for TCS025 (Tory et al. 2013),
545 which also increased the likelihood that low- θ_e air in the surrounding environment was
546 entrained into the system.

547 The TCS025 environment did not follow the steady progression of drying in the
548 mid-levels typical of the non-developing system examined by Smith and Montgomery
549 (2012) and Davis and Ahijevych (2012). There was essentially no difference in mid-level

550 θ_e between IOP-1 and IOP-3, and low-level θ_e was actually highest during IOP-3,
551 although sampling coverage may have been partly responsible for this. The large-scale
552 environment of TCS025 was modulated by TUTT cells that moved westward to the north
553 of TCS025. A trajectory analysis (not shown) indicates that the majority of the mid-level
554 low- θ_e air to the north of TCS025 during IOP-2 originated from the TUTT cell that was
555 originally to the east of TCS025. According to Komaromi (2013), the impact of mid-level
556 low- θ_e air on storm development may be greater than low- θ_e air in the lower
557 troposphere. Therefore, although vertical wind shear weakened when the TUTT cell was
558 north of TCS025, the presence of low- θ_e air in the surrounding environment appears to
559 have offset the positive impact of reduced vertical wind shear. The average mid-
560 tropospheric θ_e in both the convective and non-convective environments was lowest
561 during IOP-2, and given the large horizontal shearing deformation, some entrainment was
562 likely. This increased the negative impact potential of downdrafts (i.e., increased
563 DCAPE). Consistent with this assumption, Park and Elsberry (2013) concluded that
564 evaporative cooling and strong downdrafts counteracted low-level spin-up for TCS025
565 based upon an examination of latent heating and cooling rates retrieved from ELDORA
566 radar during IOP-3.

567 Molinari et al. (2012) hypothesized that repeated lulls in convective activity for
568 TS Edouard (2002) were a result of vertical wind shear-induced ventilation that caused
569 low- θ_e air to be transported into the boundary layer via downdrafts. It is hypothesized
570 that similar processes occurred for TCS025; strong downdrafts depleted boundary layer
571 θ_e in precipitation regions, which subsequently reduced convective intensity.
572 Alternatively, it is possible that dry air entrainment also weakened updraft intensity and

573 limited the vorticity amplification process as proposed by Smith and Montgomery (2012).
574 A convective lull occurred after MCS-G dissipated; deep convection was relatively
575 absent at the convective maximum time late on 28 August, and the next episode of deep
576 convection did not form until the system had moved a considerable distance to the north.
577 Thus, when vertical wind shear was beginning to weaken on 28 August, thermodynamic
578 conditions became less favorable such that the convective intensity diminished, and this
579 limited further development.

580 Raymond et al. (2011) examined the non-development of TCS025 along with
581 several other developing and non-developing systems. They found positive low- and mid-
582 level vorticity tendencies during IOP-2 and IOP-3, which are in basic agreement with
583 similar calculations from the SAMURAI analyses in this study (not shown), and they
584 concluded that TCS025 transitioned to a “bottom-heavy” mass flux profile by IOP-3.
585 Despite these positive indicators and a broader environment considered generally
586 favorable for formation, TCS025 failed to develop.

587 However, as Gjorgjevska and Raymond (2014) point out, a vorticity tendency
588 analysis only provides a snapshot, and may not represent the longer-term evolution of a
589 system. In fact, for several cases analyzed by Raymond et al. (2011) and Gjorgjevska
590 and Raymond (2014) that were observed over multiple days (including TCS025), the
591 calculated vorticity tendency was opposite in sign to the observed trend. Gjorgjevska
592 and Raymond (2014) also point out that a mass flux analysis may be even more
593 sensitive to sampling biases since calculation of the average vertical velocity profile
594 relies on shorter timescales and smaller horizontal scales of motion. For instance, our
595 analysis of average dropwindsonde temperature anomaly profiles did not indicate a clear

596 trend of increasing stabilization that might be expected based on the “bottom-heavy”
597 mass flux profile found by Raymond et al. (2011) during IOP-3. Therefore, depending on
598 the area sampled and the current phase of convection at the time of the observations
599 (aircraft missions in TCS025 were generally conducted after the convective diurnal
600 maximum time), a vorticity budget or mass flux analysis might represent a short-term
601 fluctuation in intensity or not be representative of the system as a whole, which could
602 lead to an incorrect assessment regarding the potential for storm formation.

603 The findings from this study suggest that convection associated with the TCS025
604 disturbance was not of sufficient intensity and was displaced too far from the circulation
605 center to reduce the appreciable vortex misalignment of TCS025. The system-relative
606 flow was larger due to the misalignment and large horizontal flow deformation suggests
607 TCS025 lacked a quasi-closed recirculation region throughout its evolution. This likely
608 allowed dry, cool, mid-level air originating from the TUTT cell to be entrained by
609 convection near the circulation before being transported into the boundary layer through
610 convective downdrafts, which acted to suppress subsequent convection. Had deep moist
611 convection continued to occur near the midlevel circulation center, vortex re-alignment or
612 the development of a new low-level circulation below the mid-level vortex (Davis and
613 Ahijevych 2012) might have occurred. A coherent vertical vortex structure (i.e., a deep
614 pouch) would have helped to limit the impacts of the mid-level low- θ_e air on 28 August,
615 while at the same time providing a protective enclosure that would allow for a more
616 efficient system-scale response to diabatic heating (Vigh and Schubert 2009) and
617 development of a warm core.

618

619 *Acknowledgements*

620 This research was funded by the National Science Foundation grant ATM-0736003 and
621 by the Office of Naval Research Marine Meteorology grants N0001413WX20824 and
622 N0001414WX20029. TCS-08 was sponsored by the Office of Naval Research Marine
623 Meteorology Program and T-PARC was sponsored by an international consortium from
624 the United States (National Science Foundation, Office of Naval Research, Naval
625 Research Laboratory, and the U.S. Air Force), Germany (DLR, Forschungszentrum
626 Karlsruhe), Japan (Japan Meteorological Agency), Korea (National Institute for
627 Meteorological Research), and Canada (Environment Canada). The role of the National
628 Center of Atmospheric Research Earth Observing Laboratory (NCAR/EOL) during the
629 field program and data management is acknowledged. MMB was supported by the
630 National Science Foundation Grant AGS-0851077 and Office of Naval Research Marine
631 Meteorology Grant N001408WR20129.

References

- Bartels, D. L., and R. A. Maddox, 1991: Midlevel cyclonic vortices generated by mesoscale convective systems. *Mon. Wea. Rev.*, **119**, 104–118.
- Bell, M. M., and M. T. Montgomery, 2010: Sheared deep vortical convection in pre-depression Hagupit during TCS08. *Geophys. Res. Lett.*, **37**, L06802, doi:10.1029/2009GL042313.
- Bell, M. M., M. T. Montgomery, and K. A. Emanuel, 2012: Air-sea enthalpy and momentum exchange at major hurricane wind speeds observed during CBLAST. *J. Atmos. Sci.*, **69**, 3197–3222.
- Bell, M. M., W.-C. Lee, C. A. Wolff, and H. Cai, 2013: A Solo-based automated quality control algorithm for airborne tail Doppler radar data. *J. Appl. Meteor. Climatol.*, **52**, 2509–2528.
- Chen, S. S., and W. M. Frank, 1993: A numerical study of the genesis of extratropical convective mesovortices. Part I: Evolution and dynamics. *J. Atmos. Sci.*, **50**, 2401–2426.
- Davis, C., C. Snyder, and A. C. Didlake, 2008: A vortex-based perspective of eastern Pacific tropical cyclone formation. *Mon. Wea. Rev.*, **136**, 2461–2477.
- Davis, C. A., and D. A. Ahijevych, 2012: Mesoscale structural evolution of three tropical weather systems observed during PREDICT. *J. Atmos. Sci.*, **69**, 1284–1305.
- Davis, C. A., and D. A. Ahijevych, 2013: Thermodynamic environments of deep convection in Atlantic tropical disturbances. *J. Atmos. Sci.*, **70**, 1912–1928.
- Davis, C. A., S. C. Jones, D. Anwender, J. Badey, and L. Scheck, 2013: Mesoscale cyclogenesis over the western North Pacific Ocean during TPARC. *Tellus A*, **65**, 18621, <http://dx.doi.org/10.3402/tellusa.v65i0.18621>.
- Dunkerton, T. J., M. T. Montgomery, and Z. Wang, 2009: Tropical cyclogenesis in a tropical wave critical layer: Easterly waves. *Atmos. Chem. Phys.*, **9**, 5587–5646.
- Elsberry, R. L., and P. A. Harr, 2008: Tropical cyclone structure (TCS08) field experiment science basis, observational platforms, and strategy. *Asia-Pacific J. Atmos. Sci.*, **44**, 209–231.
- Foerster, A. M., M. M. Bell, P. A. Harr, and S. C. Jones, 2014: Observations of the eyewall structure of Typhoon Sinlaku (2008) during the transformation stage of extratropical transition. *Mon. Wea. Rev.*, **142**, 3372–3392.
- Frank, W. M., and E. A. Ritchie, 1999: Effects of environmental flow upon tropical cyclone structure. *Mon. Wea. Rev.*, **127**, 2044–2061.

- Fu, B., M. S. Peng, T. Li, and D. E. Stevens, 2012: Developing versus nondeveloping disturbances for tropical cyclone formation. Part II: Western North Pacific*. *Mon. Wea. Rev.*, **140**, 1067–1080.
- Gjorgjevska, S., and D. J. Raymond, 2014: Interaction between dynamics and thermodynamics during tropical cyclogenesis. *Atmos. Chem. Phys.*, **14**, 3065–3082, doi:10.5194/acp-14-3065-2014, 2014.
- Gray, W. M., 1975: Tropical cyclone genesis. Dept. of Atmos. Sci. Paper No. 234, Colo. State Univ., Ft. Collins, CO, 121 pp.
- Gray, W. M., 1982: Tropical cyclone genesis and intensification. Topics in Atmospheric and Oceanographic Sciences, Intense Atmospheric Vortices, L, Bengtsson and J. Lighthill, Eds., Springer-Verlag 3-20. [ISBN 3-540-11657-5.]
- Gray, W. M., 1998: The formation of tropical cyclones. *Meteorol. Atmos. Phys.*, **67**, 37–69.
- Hildebrand, P. H., W.-C. Lee, C. A. Walther, C. Frush, M. Randall, E. Loew, R. Neitzel, R. Parsons, J. Testud, F. Baudin, and A. LeCorne, 1996: The ELDORA/ASTRAIA airborne Doppler weather radar: High-resolution observations from TOGA COARE. *Bull. Amer. Meteor. Soc.*, **77**, 213–232.
- Hock, T. F., and J. L. Franklin, 1999: The NCAR GPS dropwindsonde. *Bull. Amer. Meteor. Soc.*, **80**, 407–420.
- Houze, R. A., Jr., 2004: Mesoscale convective systems. *Rev. Geophys.*, **42**, RG4003, doi:10.1029/2004RG000150.
- Jones, S. C., 1995: The evolution of vortices in vertical shear. I: Initially barotropic vortices. *Q. J. R. Meteorol. Soc.*, **121**, 821–851.
- Komaromi, W. A., 2013: An investigation of composite dropsonde profiles for developing and nondeveloping tropical waves during the 2010 PREDICT field campaign. *J. Atmos. Sci.*, **70**, 542–558.
- Lee, C. S., 1989: Observational analysis of tropical cyclogenesis in the western North Pacific. Part I: Structural evolution of cloud clusters. *J. Atmos. Sci.*, **46**, 2580–2598.
- Lee, W.C., M. Bell, C. Wolff, E. Loew, and M. Donovan, 2009: THORPEX Pacific Asian Regional Campaign (TPARC) and Tropical Cyclone Structure (TCS08) ELDORA data quality report. NCAR/Earth Observing Laboratory, 9 pp.
- Liu, C., E. J. Zipser, and S. W. Nesbitt, 2007: Global distribution of tropical deep convection: Different perspectives from TRMM infrared and radar data. *J. Climate*, **20**, 489–503.

- Lussier, L. L., M. T. Montgomery, and M. M. Bell, 2014: The genesis of Typhoon Nuri as observed during the Tropical Cyclone Structure 2008 (TCS08) field experiment – Part 3: Dynamics of low-level spin-up during the genesis, *Atmos. Chem. Phys.*, **14**, 8795–8812, doi:10.5194/acp-14-8795-2014.
- McBride, J. L., 1981: Observational analysis of tropical cyclone formation. Part I: Basic description of data sets. *J. Atmos. Sci.*, **38**, 1117–1131.
- McBride, J. L., and R. Zehr, 1981: Observational analysis of tropical cyclone formation. Part II: Comparison of non-developing versus developing systems. *J. Atmos. Sci.*, **38**, 1132–1151.
- Molinari, J., J. Frank, and D. Vollaro, 2012: Convective bursts, downdraft cooling, and boundary layer recovery in a sheared tropical storm. *Mon. Wea. Rev.*, **141**, 1048–1060.
- Montgomery, M. T., L. L. Lussier III, R. W. Moore, and Z. Wang, 2010: The genesis of Typhoon Nuri as observed during the tropical cyclone structure 2008 (TCS-08) field experiment - Part 1: The role of the easterly wave critical layer. *Atmos. Chem. Phys.*, **10**, 9879–9900.
- Montgomery, M. T., C. Davis, T. Dunkerton, Z. Wang, C. Velden, R. Torn, S. J. Majumdar, F. Zhang, R. K. Smith, L. Bosart, M. M. Bell, J. S. Haase, A. Heymsfield, J. Jensen, T. Campos, and M. A. Boothe, 2012: The Pre-Depression Investigation of Cloud-Systems in the Tropics (PREDICT) experiment: Scientific basis, new analysis tools, and some first results. *Bull. Amer. Meteor. Soc.*, **93**, 153–172.
- Park, M.-S., C.-H. Ho, J. Kim, and R. Elsberry, 2011: Diurnal circulations and their multi-scale interaction leading to rainfall over the South China Sea upstream of the Philippines during intraseasonal monsoon westerly wind bursts. *Climate Dynam.*, **37**, 1483–1499.
- Park, M.-S., and R. L. Elsberry, 2013: Latent heating and cooling rates in developing and nondeveloping tropical disturbances during TCS-08: TRMM PR versus ELDORA retrievals. *J. Atmos. Sci.*, **70**, 15–35.
- Penny, A. B., 2013: Observations and high-resolution numerical simulations of a non-developing tropical disturbance in the western North Pacific, PhD Dissertation, Naval Postgraduate School, Monterey, CA, USA, 287 pp, Available at <http://hdl.handle.net/10945/37691>.
- Raymond, D. J., and H. Jiang, 1990: A theory for long-lived mesoscale convective systems. *J. Atmos. Sci.*, **47**, 3067–3077.
- Raymond, D. J., and S. L. Sessions, 2007: Evolution of convection during tropical cyclogenesis. *Geophys. Res. Lett.*, **34**, L06811, doi:10.1029/2006GL028607.

- Raymond, D. J., and C. López Carrillo, 2011: The vorticity budget of developing Typhoon Nuri (2008). *Atmos. Chem. Phys.*, **11**, 147–163.
- Raymond, D. J., S. L. Sessions, and C. López Carrillo, 2011: Thermodynamics of tropical cyclogenesis in the northwest Pacific. *J. Geophys. Res.*, **116**, D18101, doi:10.1029/2011JD015624.
- Simpson, J., E. Ritchie, G. J. Holland, J. Halverson, and S. Stewart, 1997: Mesoscale interactions in tropical cyclone genesis. *Mon. Wea. Rev.*, **125**, 2643–2661.
- Smith, R. K., and M. T. Montgomery, 2012: Observations of the convective environment in developing and non-developing tropical disturbances. *Q. J. R. Meteorol. Soc.*, doi:10.1002/qj.1910.
- Testud, J., P. H. Hildebrand, and W.-C. Lee, 1995: A procedure to correct airborne Doppler radar data for navigation errors using the echo returned from the earth's surface. *J. Atmos. Oceanic Technol.*, **12**, 800–820.
- Tory, K. J., M. T. Montgomery, and N. E. Davidson, 2006: Prediction and diagnosis of tropical cyclone formation in an NWP system. Part I: The critical role of vortex enhancement in deep convection. *J. Atmos. Sci.*, **63**, 3077–3090.
- Tory, K. J., R. A. Dare, N. E. Davidson, J. L. McBride, and S. S. Chand, 2013: The importance of low-deformation vorticity in tropical cyclone formation. *Atmos. Chem. Phys.*, **13**, 2115–2132, doi:10.5194/acp-13-2115-2013.
- Uhlhorn, E. W., P. G. Black, J. L. Franklin, M. Goodberlet, J. Carswell, and A. S. Goldstein, 2007: Hurricane surface wind measurements from an operational stepped frequency microwave radiometer. *Mon. Wea. Rev.*, **135**, 3070–3085.
- Vigh, J. L., and W. H. Schubert, 2009: Rapid development of the tropical cyclone warm core. *J. Atmos. Sci.*, **66**, 3335–3350.
- Wakimoto, R. M., W.-C. Lee, H. B. Bluestein, C.-H. Liu, and P. H. Hildebrand, 1996: ELDORA observations during VORTEX 95. *Bull. Amer. Meteor. Soc.*, **77**, 1465–1481.
- Waliser, D. E., and Coauthors, 2012: The “year” of tropical convection (May 2008 to April 2010): Climate variability and weather highlights. *Bull. Amer. Meteor. Soc.*, **93**, 1189–1218.
- Yang, S., and E. A. Smith, 2006: Mechanisms for diurnal variability of global tropical rainfall observed from TRMM. *J. Climate*, **19**, 5190–5226.
- Young, K., J. Wang, and D. Lauritsen, 2009a: THORPEX Pacific Regional Campaign (TPARC) 2008 Quality Controlled Air Force C-130 Dropsonde Data Set. NCAR/Earth Observing Laboratory, 9 pp, available at

<http://data.eol.ucar.edu/datafile/nph-get/110.085/readme.TPARC2008-C130.dropsondes.doc>.

Young, K., J. Wang, and D. Lauritsen, 2009b: THORPEX Pacific Regional Campaign (TPARC) 2008 Quality Controlled NRL-P3 Dropsonde Data Set. NCAR/Earth Observing Laboratory, 9 pp, available at <http://data.eol.ucar.edu/datafile/nph-get/110.078/readme.TPARC2008-P3.dropsondes.doc>

Figure Captions

Figure 1: Approximate on-station (data collection) times for TCS025 aircraft missions 0125W – 0525W. Numbers in parentheses correspond to the number of dropwindsondes deployed during each mission.

Figure 2: (a) Tracks of MCSs during TCS025 with open and closed circles indicating the formation and dissipation locations, respectively. The solid and dashed black lines mark the 850 hPa earth-relative circulation center and vorticity maximum tracks, respectively, which are based on a ECMWF analysis (see text for details) and are labeled at 0000 UTC positions (black circles). The approximate duration for each MCS is listed in the inset in (a) and shown as a time series in (b).

Figure 3: (a) MTSAT IR brightness temperature ($^{\circ}\text{C}$) at 2345 UTC 26 August. Horizontal wind vectors (m s^{-1} , colored scale on right) and geopotential heights (m, black contours) at (b) 200 hPa and (c) 850 hPa from ECMWF analysis valid at 0000 UTC 27 August. The location of MCS-D is annotated in (a) and the red line and red circles in (b) and (c) correspond to the flight track and dropwindsonde deployment locations for WC-130J flight 0125W. Low-level circulations are labeled L1, L2, and L3 in (a) and (c) and G marks the location of Guam.

Figure 4: As in Fig. 3, except (a) MTSAT IR brightness temperature at 2345 UTC 27 August and ECMWF analysis valid at 0000 UTC 28 August. The location of MCS-G is annotated in (a) and the red line and red circles in (b) and (c) correspond to the flight

track and dropwindsonde deployment locations for WC-130J flight 0325W. Blue line and blue circles in (b) and (c) correspond to the flight track and dropwindsonde deployment locations for P-3 flight 0225W. South to north vertical cross section shown in Fig. 14 is marked by black line in (b) and (c).

Figure 5: As in Fig. 3, except (a) MTSAT IR brightness temperature at 2345 UTC 28 August and ECMWF analysis valid at 0000 UTC 29 August. Red line and red circles in (b) and (c) correspond to the flight track and dropwindsonde deployment locations for WC-130J flight 0525W. Blue line and blue circles in (b) and (c) correspond to the flight track and dropwindsonde deployment locations for P-3 flight 0425W.

Figure 6: As in Fig. 3, except (a) MTSAT-IR brightness temperature valid at 2345 UTC 29 August and ECMWF analysis valid at 0000 UTC 30 August.

Figure 7: (a) Deep layer (200-850 hPa, green, kt) and low- to mid-level (500-850 hPa, purple, kt) environmental vertical wind shear and direction (wind barbs, 1 full barb = 10 kt) computed using the ECMWF analysis (see text for details). Also shown are wind barbs for the pseudo-aligned (blue barb, 5.4 kt) and misaligned (red barb, 9.3 kt) mesoscale system-relative flow from the 0000 UTC 28 August SAMURAI analysis (see text for details). (b) Time series of the box-average ($\pm 3^\circ$ from vorticity maxima locations) normalized Okubo-Weiss parameter from the ECMWF analysis at pressure levels shown in inset.

Figure 8: Ratio expressed as a percentage of area with MTSAT-IR brightness temperatures less than -65°C to that less than -35°C for MCSs that developed within the environment of TCS025. Dashed vertical black lines indicate the approximate time of the expected early morning convective maximum.

Figure 9: Radially averaged (0° - 3°) half-hourly MTSAT IR brightness temperatures ($^{\circ}\text{C}$, shading) relative to the ECMWF 850 hPa vorticity maximum positions of TCS025. Colored bands along the ordinate represent WC-130J and P-3 aircraft missions flown into TCS025 with brown, blue and orange corresponding to the WC-130J missions and red and green to the P-3 missions. Abscissa axis labels correspond to directions along the azimuth. Short dashed horizontal lines mark the approximate time of diurnal convective maximum (1800 UTC) and long dashed horizontal line denotes the ending time of the 0225W P-3 mission. The brightness temperature features associated with MCS-D and MCS-G are annotated.

Figure 10: MTSAT IR brightness temperature ($^{\circ}\text{C}$, shading) at 2345 UTC 26 August. The WC-130J flight track (black line) and dropwindsonde deployment locations (white circles) are shown with wind barbs corresponding to 1500 m height (1 full barb = 10 kt) for IOP-1 (0125W).

Figure 11: MTSAT IR brightness temperature ($^{\circ}\text{C}$, shading) at 2345 UTC 27 August. The WC-130J flight track (black line), P-3 flight track (red line), and dropwindsonde deployment locations (white circles) are shown with wind barbs corresponding to 1500 m

height (1 full barb = 10 kt) for IOP-2 (0225W and 0325W). Red-filled dropwindsonde locations near 151°E were used in the vertical cross section in Fig. 16, and the red-filled star denotes the dropwindsonde deployed at 0046 UTC. The bold black line near 151.8°E denotes the location of the cross-section in Fig. 14. Black dashed portion of the WC-130J flight track corresponds with the locations where SFMR rain rate and IR brightness temperature data were analyzed in Fig. 17.

Figure 12: Storm-relative WC-130J (0325W: 2103 UTC 27 August – 0407 UTC 28 August) and P-3 (0225W: 0130 UTC 28 August – 0520 UTC 28 August) flight tracks for IOP-2 in TCS025. Small black dots denote dropwindsonde locations and wind barbs correspond to heights shown in legend (1 full barb = 10 kt). Colored circles with black outlines connected with the dashed black line mark dropwindsonde-derived circulation center locations at heights listed in inset. Solid colored circles connected by a solid black line mark the circulation center locations at heights listed in inset obtained from the SAMURAI streamline analysis.

Figure 13: Storm-relative wind speed (kt, shading) and vectors (m s^{-1}) at (a) 5 km and (b) 1.5 km from the 5-km SAMURAI analysis valid at 0000 UTC 28 August. The WC-130J track for flight 0325W is in red and the P-3 track for flight 0225W is in blue. Black wind barbs (1 full barb = 10 kt) correspond to dropwindsonde winds corrected for storm motion. Solid black line denotes location of the cross-section in Fig. 14. The $2^{\circ} \times 2^{\circ}$ black and red boxes are centered on the circulation center positions at 1.5 (black dot) and

5 km (red dot), respectively, are used in the mesoscale vertical wind shear calculations in Fig. 7 and discussed in text.

Figure 14: South-to-north oriented vertical cross section of relative vorticity (10^{-5} s^{-1} , shading), divergence (10^{-5} s^{-1} , black contours at $4.0 \times 10^{-5} \text{ s}^{-1}$ intervals with negative values dashed), θ_e (K, blue contours for $\theta_e \leq 340 \text{ K}$), and wind vectors in the plane of the cross section (m s^{-1}) constructed from (a) the ECMWF background field and (b) the SAMURAI analysis with 5-km grid spacing valid at 0000 UTC 28 August. The location of cross section corresponds to solid black lines shown in Figs. 4, 11, 13, and 15. Thick vertical black lines immediately below the abscissa in (b) correspond to southern and northern extent of ELDORA Doppler radar at the longitude of the cross-section (see Fig. 15).

Figure 15: ELDORA reflectivity (dBZ, shading) at 5-km height from the P-3 flight 0225W early on 28 August. The white horizontal wind vectors (m s^{-1} , with 15 m s^{-1} reference vector indicated at top right) correspond to the wind field at 5-km height derived using the SAMURAI analysis technique with 2-km grid spacing. The WC-130J track for flight 0325W is in red and the P-3 track for flight 0225W is in blue. Black wind barbs correspond to dropwindsonde winds corrected for storm motion (1 full barb = 10 kt). The solid black line denotes the location of the cross-section in Fig. 14.

Figure 16: South-to-north vertical cross section of equivalent potential temperature (K) constructed using dropwindsonde data (red-filled circles in Fig. 11) collected during the

second WC-130J flight (0325W). Wind barbs depict the dropwindsonde horizontal wind (1 full barb = 10 kt) and have been oriented to match the cross section such that wind barbs pointing from right to left correspond with northerly winds.

Figure 17: SFMR rain rate (mm h^{-1} , blue line and left ordinate) and MTSAT IR brightness temperatures ($^{\circ}\text{C}$, red line and right ordinate) interpolated spatially and temporally to the flight track during the second WC-130J flight (0325W) from 0000 UTC – 0200 UTC 28 August. Abscissa axis labels correspond to UTC time. Black dashed line in Fig. 11 denotes the location along the flight track corresponding to this time interval. The black circle along the abscissa indicates the time of the 0046 UTC dropwindsonde in Fig. 16.

Figure 18: MTSAT IR brightness temperature ($^{\circ}\text{C}$, shading) valid at 2345 UTC 28 August with flight tracks for the WC-130J (black line) and P-3 (red line), dropwindsonde deployment locations (white circles), and horizontal dropwindsonde winds at 1.5 km height (1 full barb = 10 kt) for IOP-3 (0425W and 0525W) in the ground-relative frame. (b) As in panel (a), except for storm-relative wind speed (kt, shading) and vectors (m s^{-1}) at 1.5 km height from the 5-km SAMURAI analysis valid at 0000 UTC 29 August. Flight tracks, dropwindsonde deployment locations, and dropwindsonde winds have been adjusted for storm motion in (b).

Figure 19: Vertical profiles of (a) relative humidity (%), (b) θ_e (K), and (c) DCAPE (J kg^{-1}) averaged for dropwindsondes for which the MTSAT IR brightness temperatures

interpolated to the dropwindsonde time and location were less than -35°C (solid lines) and greater than -35°C (dashed lines) during WC-130J aircraft missions shown in inset. The average MTSAT IR brightness temperatures of dropwindsondes used to compute each average are shown in inset. (d) Vertical profiles of temperature anomaly (K) from dropwindsondes averaged within 250 km of the analyzed ECMWF 850 hPa circulation center during aircraft missions shown in inset. Each mean profile used to compute the average temperature anomaly was constructed from all dropwindsondes from each flight. The number of dropwindsondes used to compute each average is shown in the inset of each figure.

Figure 20: Equivalent potential temperature (K, shading), geopotential height (m, contours), and storm-relative wind vectors (m s^{-1} , with 10 m s^{-1} reference vector indicated at bottom right in panel-d) at 500 hPa from the ECMWF analysis at times annotated in each panel.

Figures

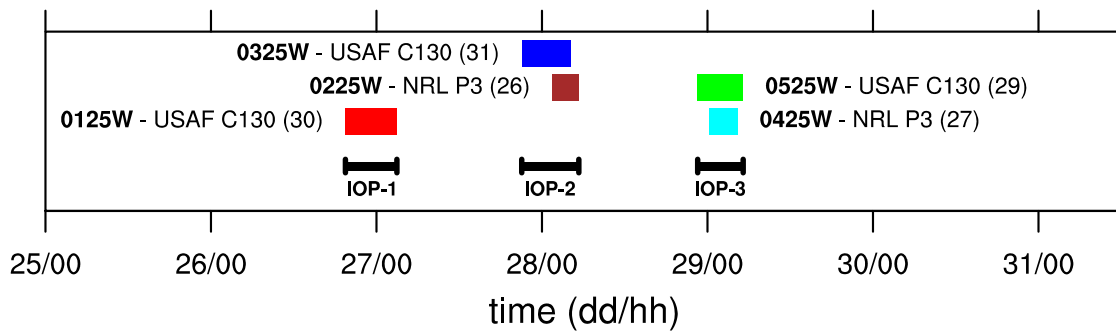


Figure 1: Approximate on-station (data collection) times for TCS025 aircraft missions 0125W – 0525W. Numbers in parentheses correspond to the number of dropwindsondes deployed during each mission.

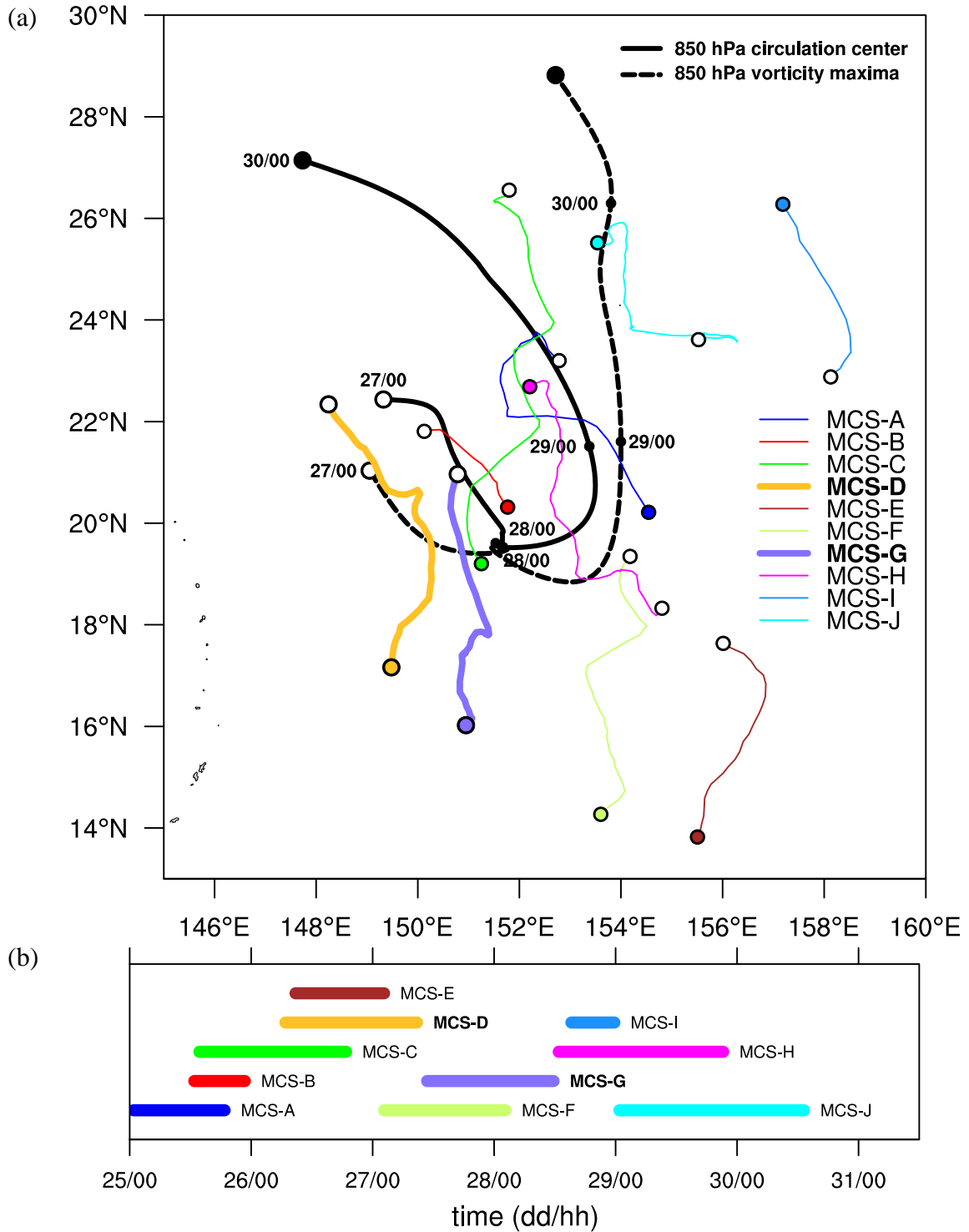


Figure 2: (a) Tracks of MCSs during TCS025 with open and closed circles indicating the formation and dissipation locations, respectively. The solid and dashed black lines mark the 850 hPa earth-relative circulation center and vorticity maximum tracks, respectively, which are based on a ECMWF analysis (see text for details) and are labeled at 0000 UTC positions (black circles). The approximate duration for each MCS is listed in the inset in (a) and shown as a time series in (b).

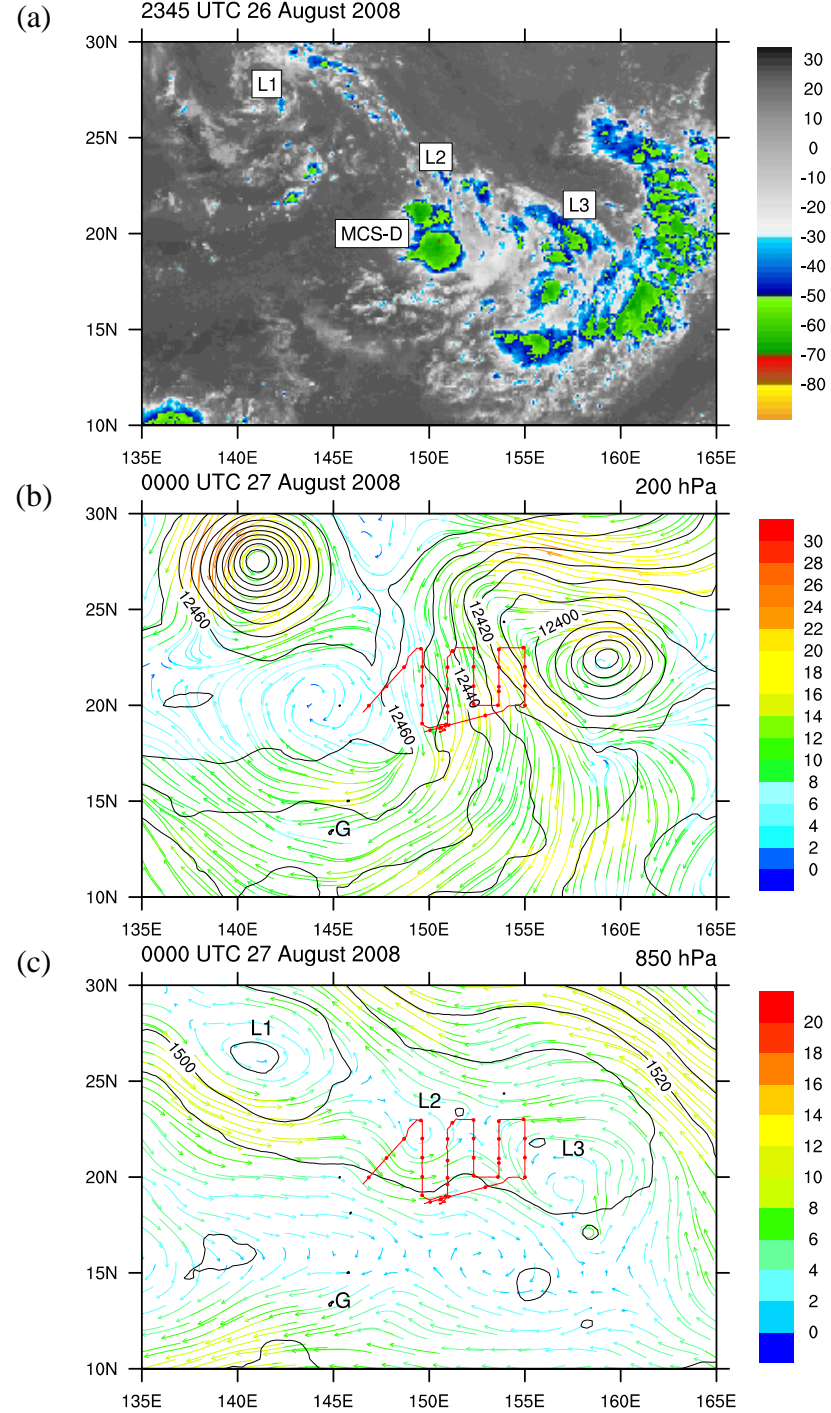


Figure 3: (a) MTSAT IR brightness temperature ($^{\circ}\text{C}$) at 2345 UTC 26 August. Horizontal wind vectors (m s^{-1} , colored scale on right) and geopotential heights (m, black contours) at (b) 200 hPa and (c) 850 hPa from ECMWF analysis valid at 0000 UTC 27 August. The location of MCS-D is annotated in (a) and the red line and red circles in (b) and (c) correspond to the flight track and dropwindsonde deployment locations for WC-130J flight 0125W. Low-level circulations are labeled L1, L2, and L3 in (a) and (c) and G marks the location of Guam.

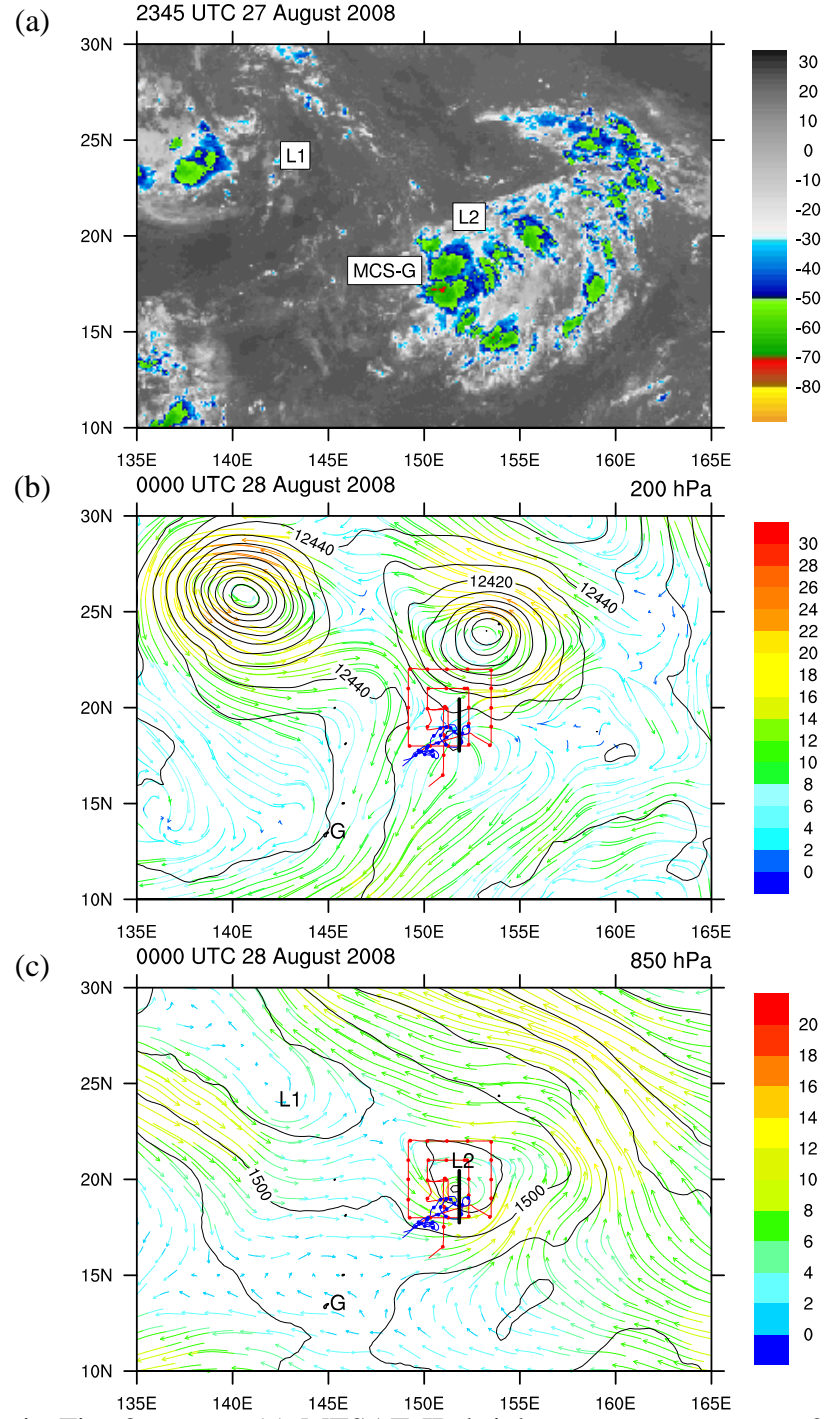


Figure 4: As in Fig. 3, except (a) MTSAT IR brightness temperature at 2345 UTC 27 August and ECMWF analysis valid at 0000 UTC 28 August. The location of MCS-G is annotated in (a) and the red line and red circles in (b) and (c) correspond to the flight track and dropwindsonde deployment locations for WC-130J flight 0325W. Blue line and blue circles in (b) and (c) correspond to the flight track and dropwindsonde deployment locations for P-3 flight 0225W. South to north vertical cross section shown in Fig. 14 is marked by black line in (b) and (c).

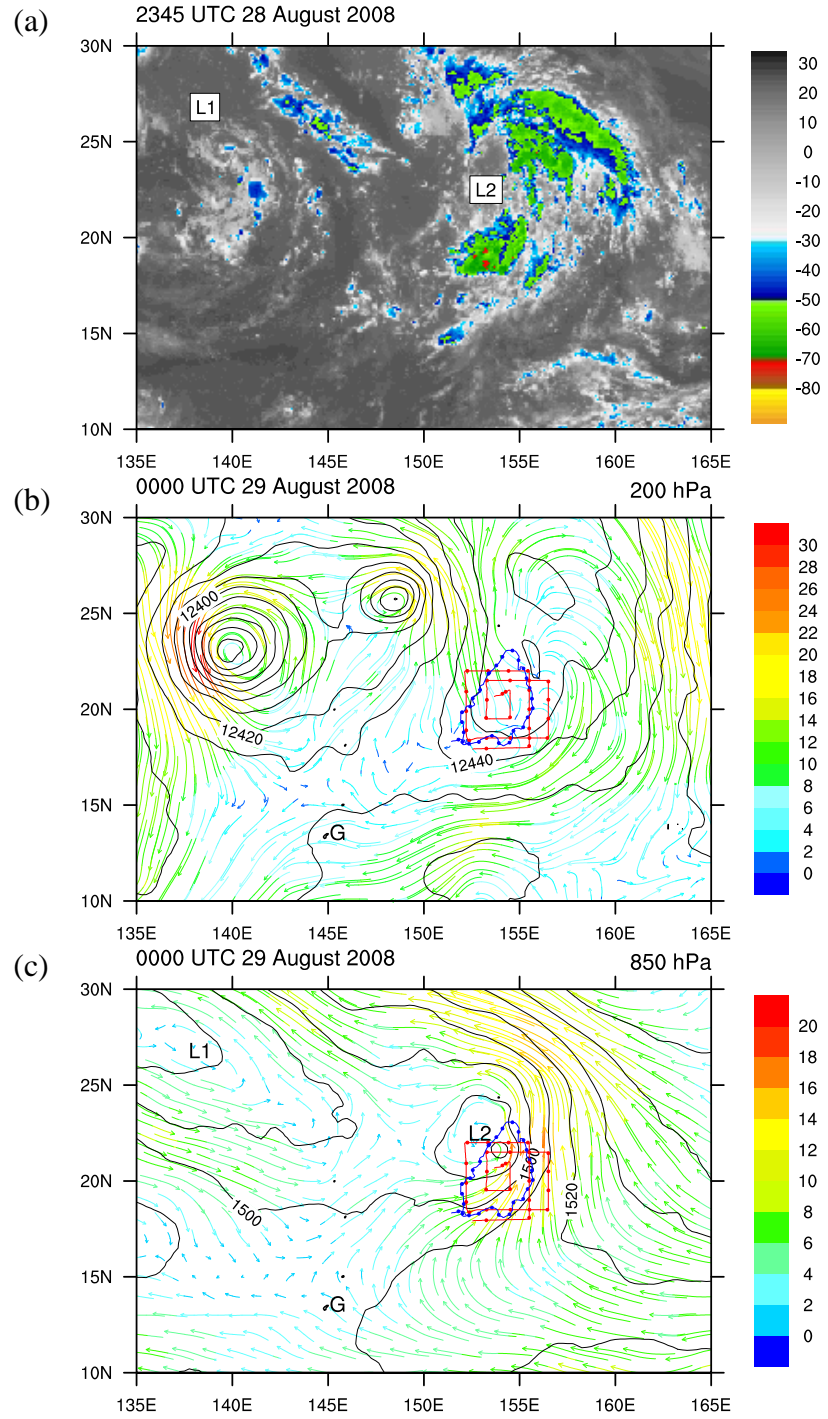


Figure 5: As in Fig. 3, except (a) MTSAT IR brightness temperature at 2345 UTC 28 August and ECMWF analysis valid at 0000 UTC 29 August. Red line and red circles in (b) and (c) correspond to the flight track and dropwindsonde deployment locations for WC-130J flight 0525W. Blue line and blue circles in (b) and (c) correspond to the flight track and dropwindsonde deployment locations for P-3 flight 0425W.

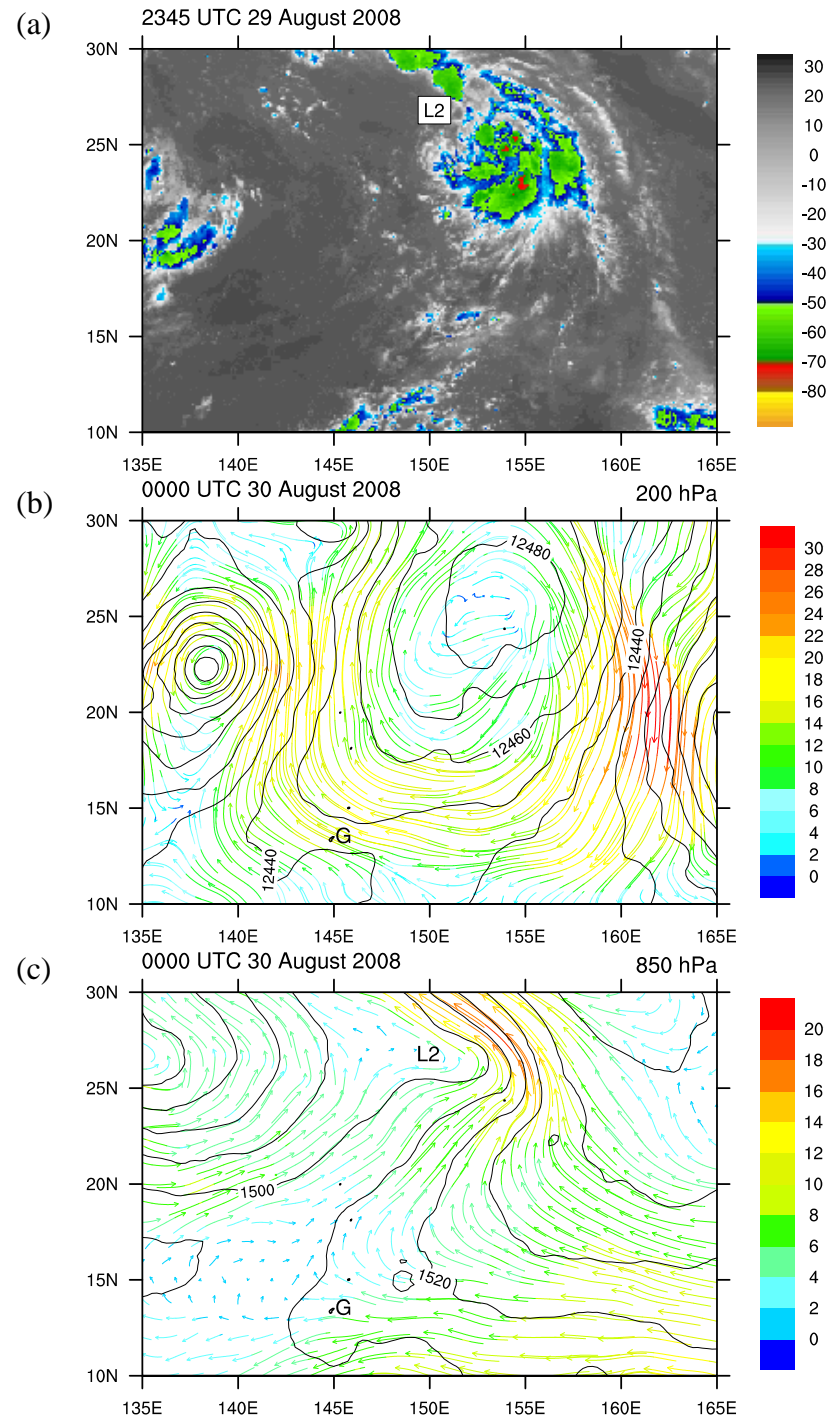


Figure 6: As in Fig. 3, except (a) MTSAT-IR brightness temperature valid at 2345 UTC 29 August and ECMWF analysis valid at 0000 UTC 30 August.

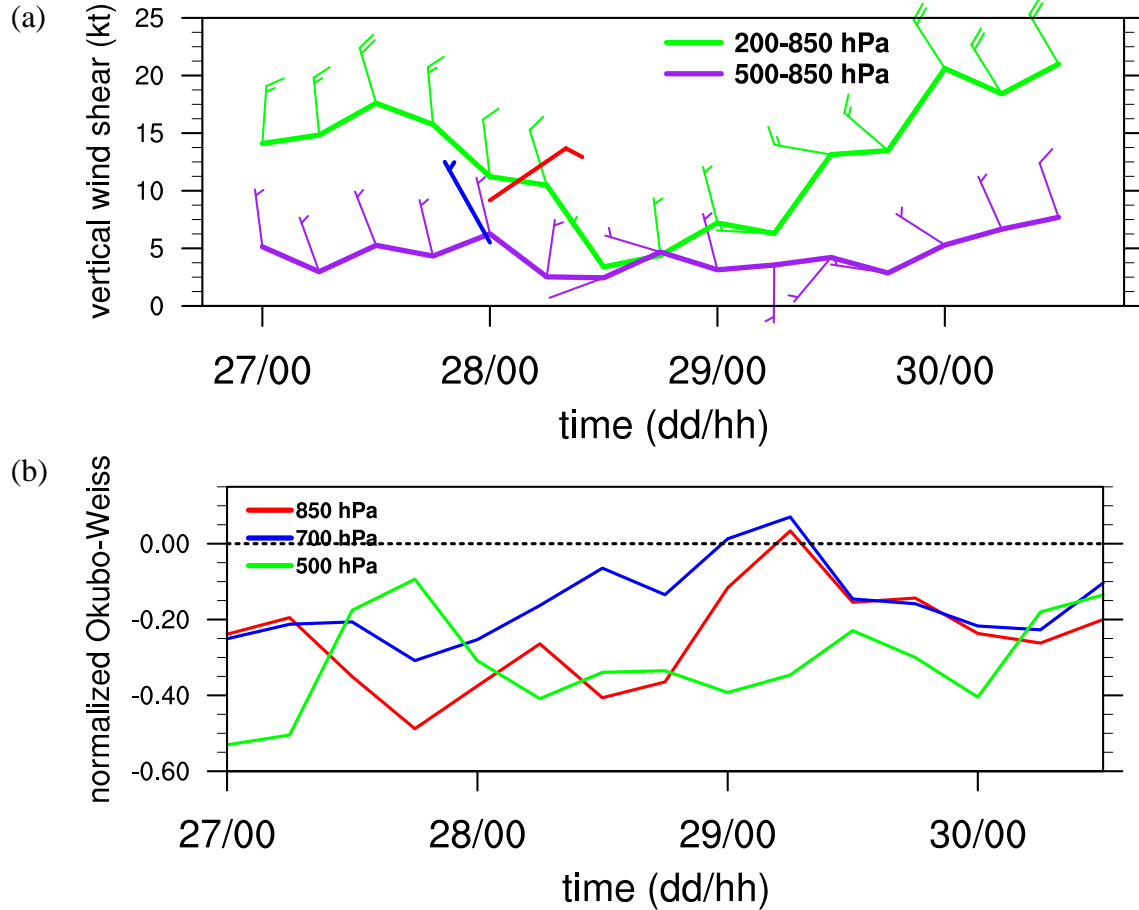


Figure 7: (a) Deep layer (200-850 hPa, green, kt) and low- to mid-level (500-850 hPa, purple, kt) environmental vertical wind shear and direction (wind barbs, 1 full barb = 10 kt) computed using the ECMWF analysis (see text for details). Also shown are wind barbs for the pseudo-aligned (blue barb, 5.4 kt) and misaligned (red barb, 9.3 kt) mesoscale system-relative flow from the 0000 UTC 28 August SAMURAI analysis (see text for details). (b) Time series of the box-average ($\pm 3^\circ$ from vorticity maxima locations) normalized Okubo-Weiss parameter from the ECMWF analysis at pressure levels shown in inset.

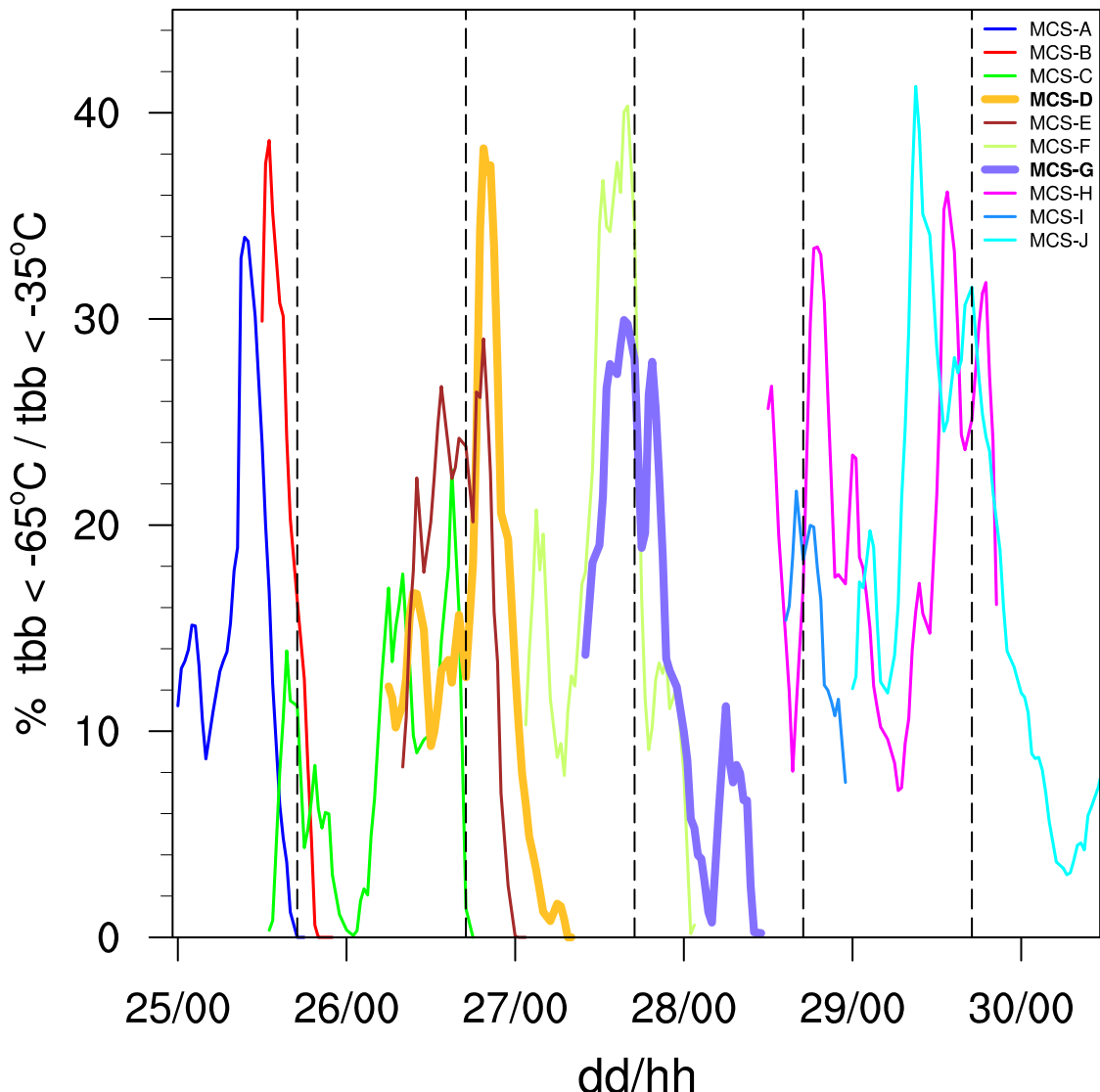


Figure 8: Ratio expressed as a percentage of area with MTSAT-IR brightness temperatures less than -65°C to that less than -35°C for MCSs that developed within the environment of TCS025. Dashed vertical black lines indicate the approximate time of the expected early morning convective maximum.

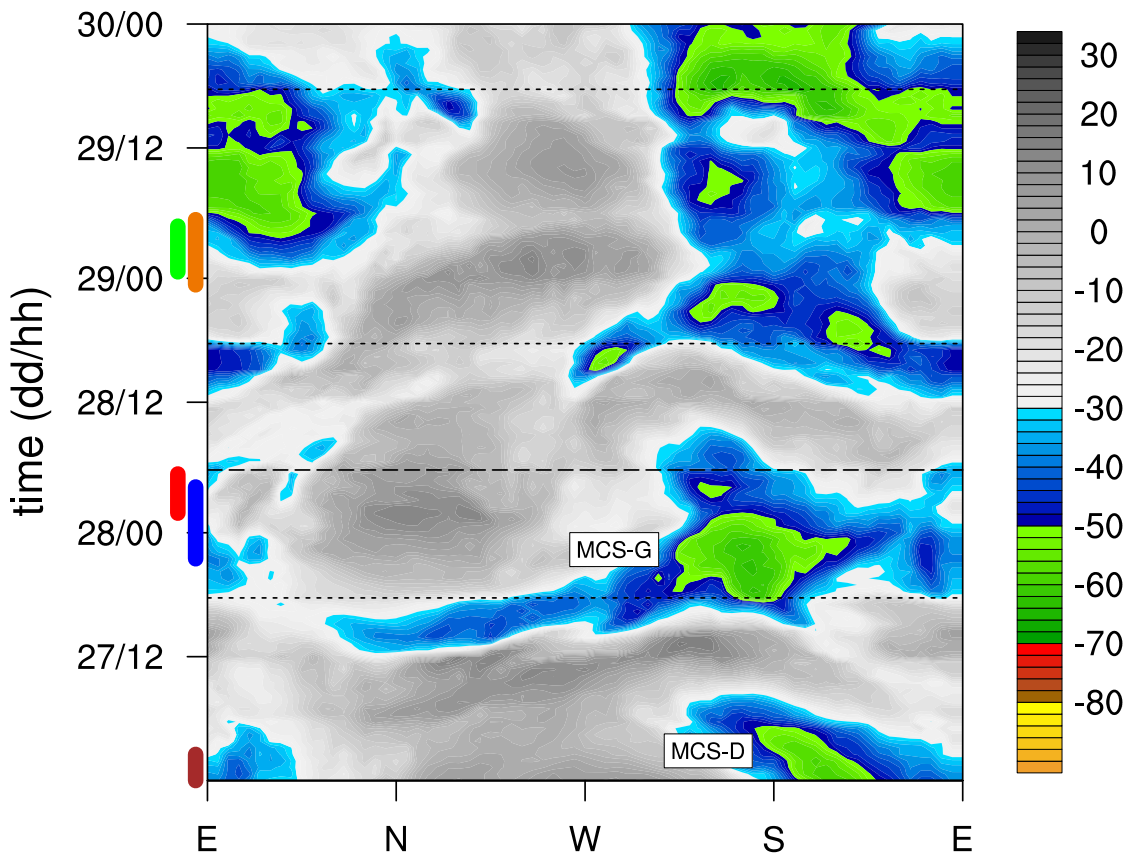


Figure 9: Radially averaged (0° - 3°) half-hourly MTSAT IR brightness temperatures ($^{\circ}\text{C}$, shading) relative to the ECMWF 850 hPa vorticity maximum positions of TCS025. Colored bands along the ordinate represent WC-130J and P-3 aircraft missions flown into TCS025 with brown, blue and orange corresponding to the WC-130J missions and red and green to the P-3 missions. Abscissa axis labels correspond to directions along the azimuth. Short dashed horizontal lines mark the approximate time of diurnal convective maximum (1800 UTC) and long dashed horizontal line denotes the ending time of the 0225W P-3 mission. The brightness temperature features associated with MCS-D and MCS-G are annotated.

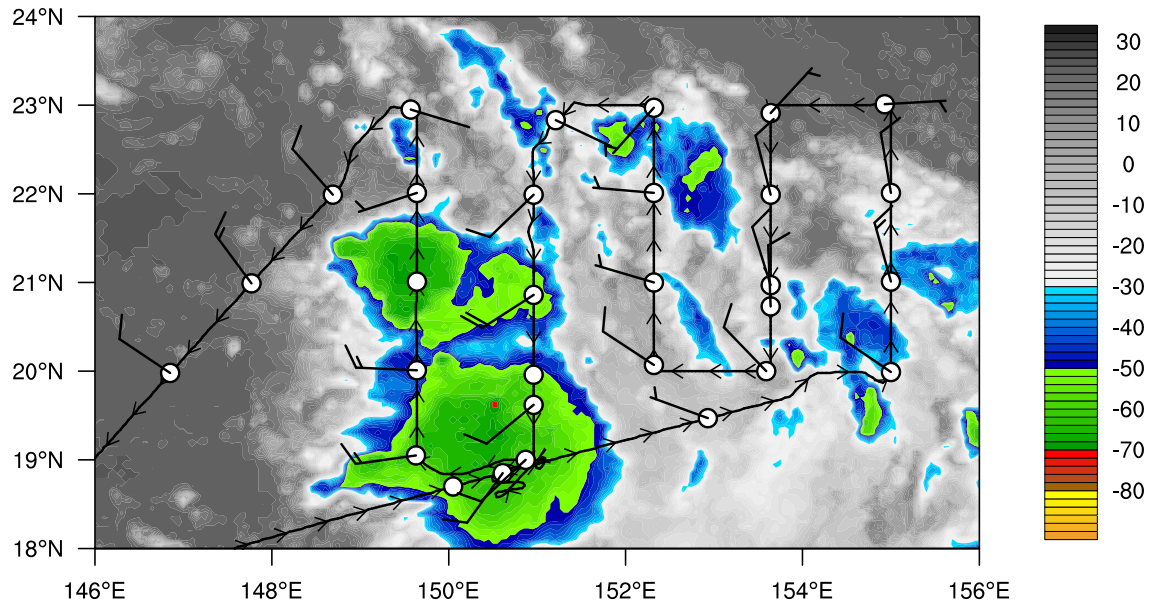


Figure 10: MTSAT IR brightness temperature ($^{\circ}\text{C}$, shading) at 2345 UTC 26 August. The WC-130J flight track (black line) and dropwindsonde deployment locations (white circles) are shown with wind barbs corresponding to 1500 m height (1 full barb = 10 kt) for IOP-1 (0125W).

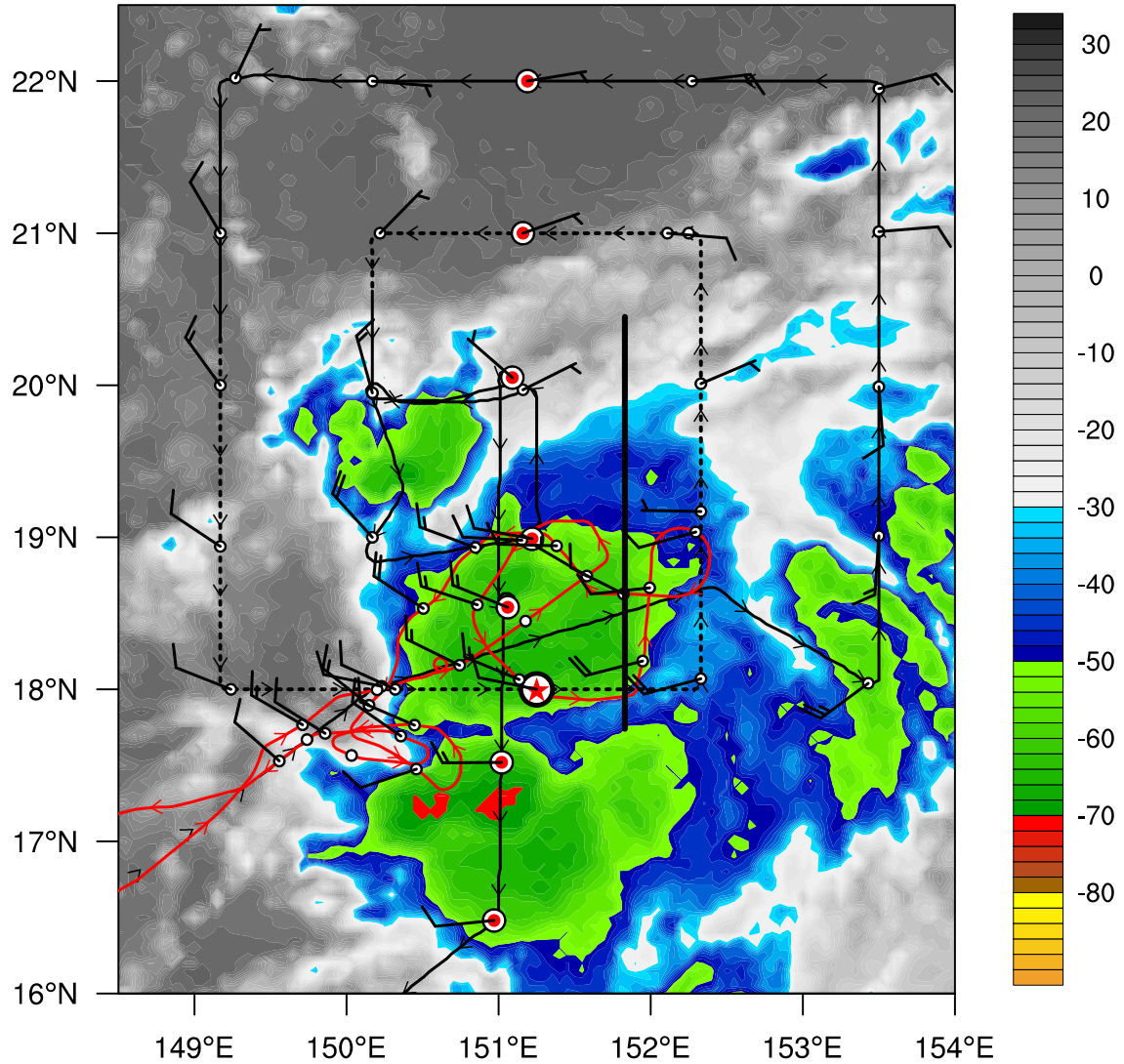


Figure 11: MTSAT IR brightness temperature ($^{\circ}\text{C}$, shading) at 2345 UTC 27 August. The WC-130J flight track (black line), P-3 flight track (red line), and dropwindsonde deployment locations (white circles) are shown with wind barbs corresponding to 1500 m height (1 full barb = 10 kt) for IOP-2 (0225W and 0325W). Red-filled dropwindsonde locations near 151°E were used in the vertical cross section in Fig. 16, and the red-filled star denotes the dropwindsonde deployed at 0046 UTC. The bold black line near 151.8°E denotes the location of the cross-section in Fig. 14. Black dashed portion of the WC-130J flight track corresponds with the locations where SFMR rain rate and IR brightness temperature data were analyzed in Fig. 17.

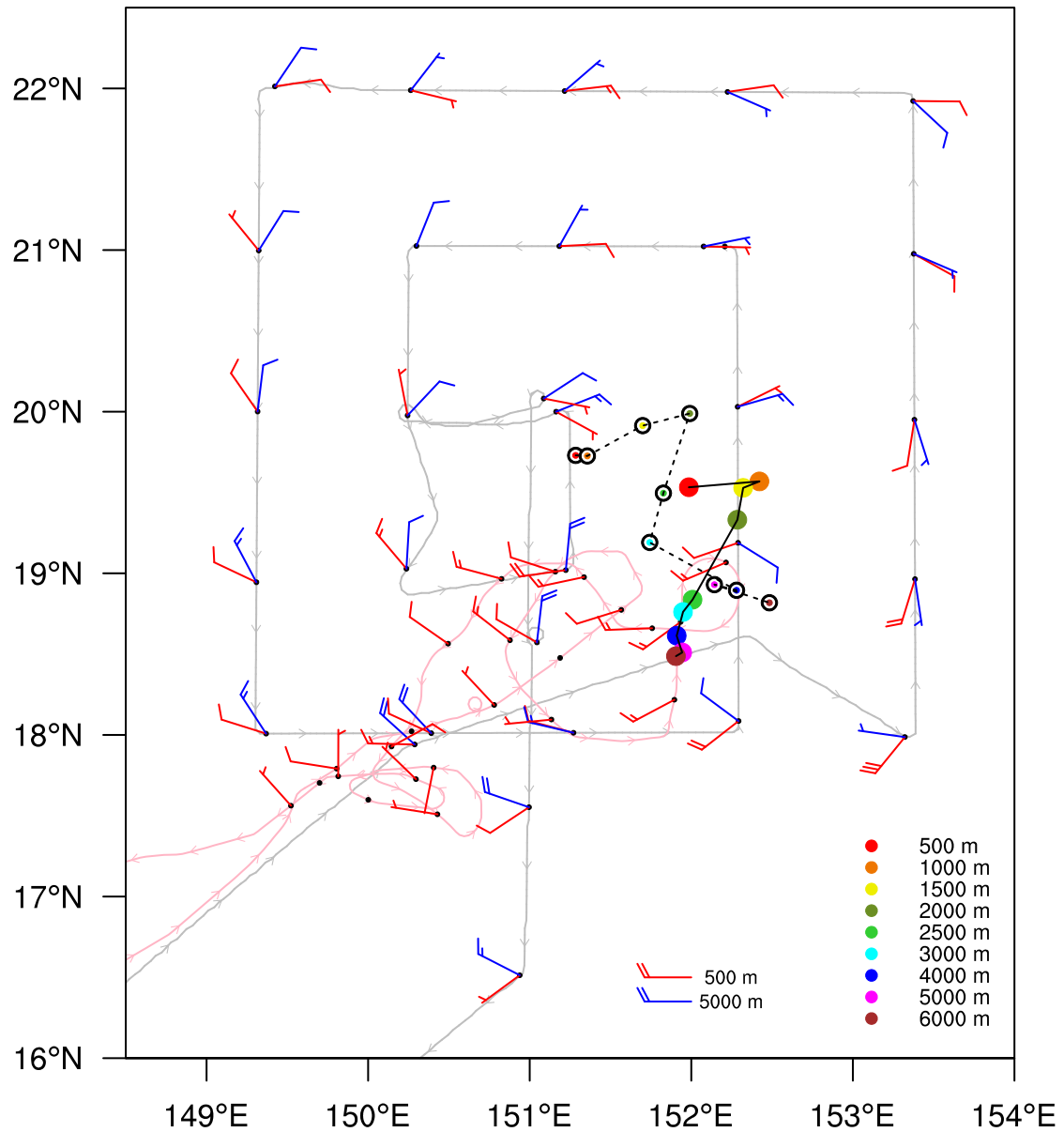


Figure 12: Storm-relative WC-130J (0325W: 2103 UTC 27 August – 0407 UTC 28 August) and P-3 (0225W: 0130 UTC 28 August – 0520 UTC 28 August) flight tracks for IOP-2 in TCS025. Small black dots denote dropwindsonde locations and wind barbs correspond to heights shown in legend (1 full barb = 10 kt). Colored circles with black outlines connected with the dashed black line mark dropwindsonde-derived circulation center locations at heights listed in inset. Solid colored circles connected by a solid black line mark the circulation center locations at heights listed in inset obtained from the SAMURAI streamline analysis.

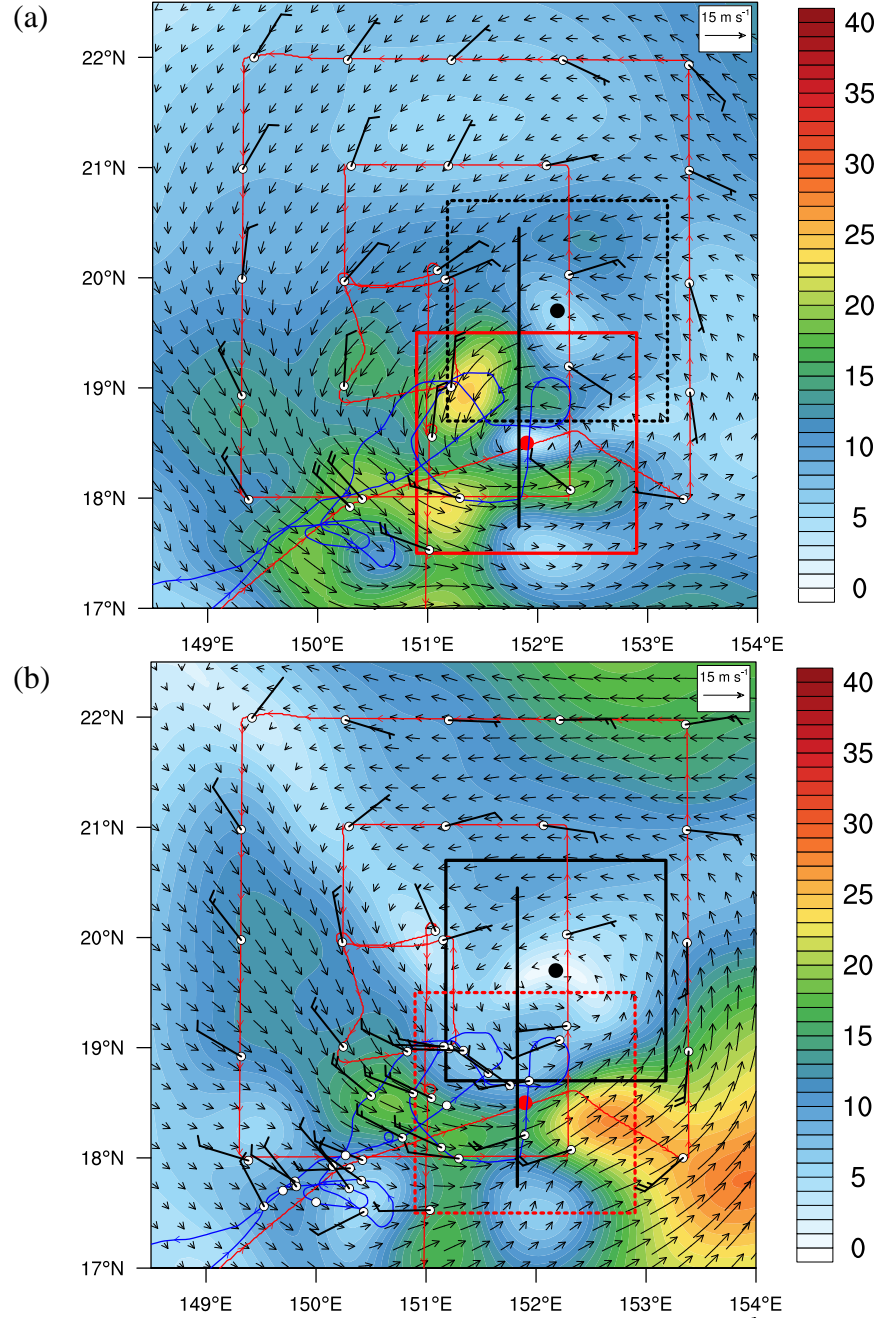


Figure 13: Storm-relative wind speed (kt, shading) and vectors (m s^{-1}) at (a) 5 km and (b) 1.5 km from the 5-km SAMURAI analysis valid at 0000 UTC 28 August. The WC-130J track for flight 0325W is in red and the P-3 track for flight 0225W is in blue. Black wind barbs (1 full barb = 10 kt) correspond to dropwindsonde winds corrected for storm motion. Solid black line denotes location of the cross-section in Fig. 14. The $2^\circ \times 2^\circ$ black and red boxes are centered on the circulation center positions at 1.5 (black dot) and 5 km (red dot), respectively, are used in the mesoscale vertical wind shear calculations in Fig. 7 and discussed in text.

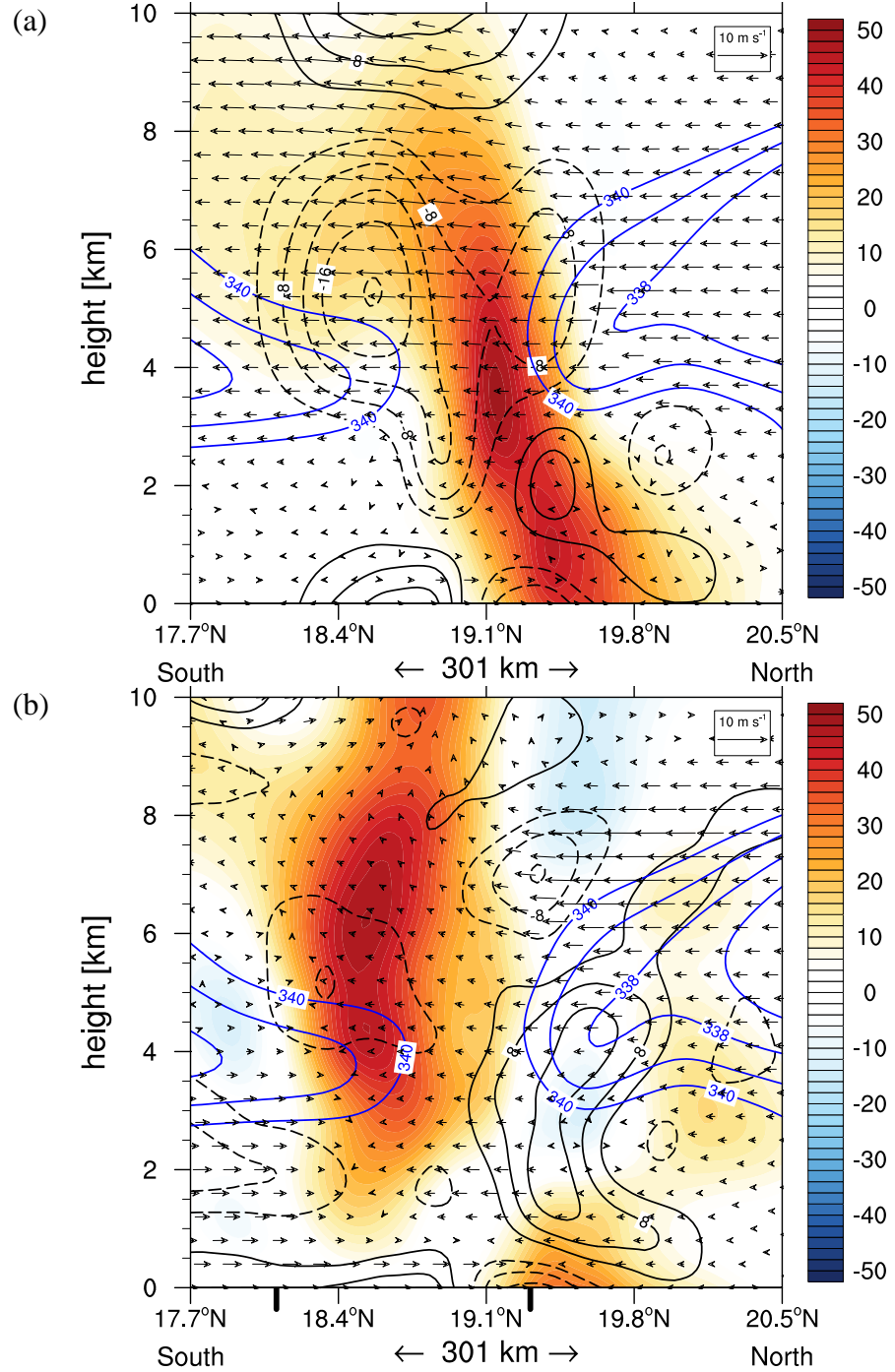


Figure 14: South-to-north oriented vertical cross section of relative vorticity (10^{-5} s^{-1} , shading), divergence (10^{-5} s^{-1} , black contours at $4.0 \times 10^{-5} \text{ s}^{-1}$ intervals with negative values dashed), θ_e (K, blue contours for $\theta_e \leq 340 \text{ K}$), and wind vectors in the plane of the cross section (m s^{-1}) constructed from (a) the ECMWF background field and (b) the SAMURAI analysis with 5-km grid spacing valid at 0000 UTC 28 August. The location of cross section corresponds to solid black lines shown in Figs. 4, 11, 13, and 15. Thick vertical black lines immediately below the abscissa in (b) correspond to southern and northern extent of ELDORA Doppler radar at the longitude of the cross-section (see Fig. 15).

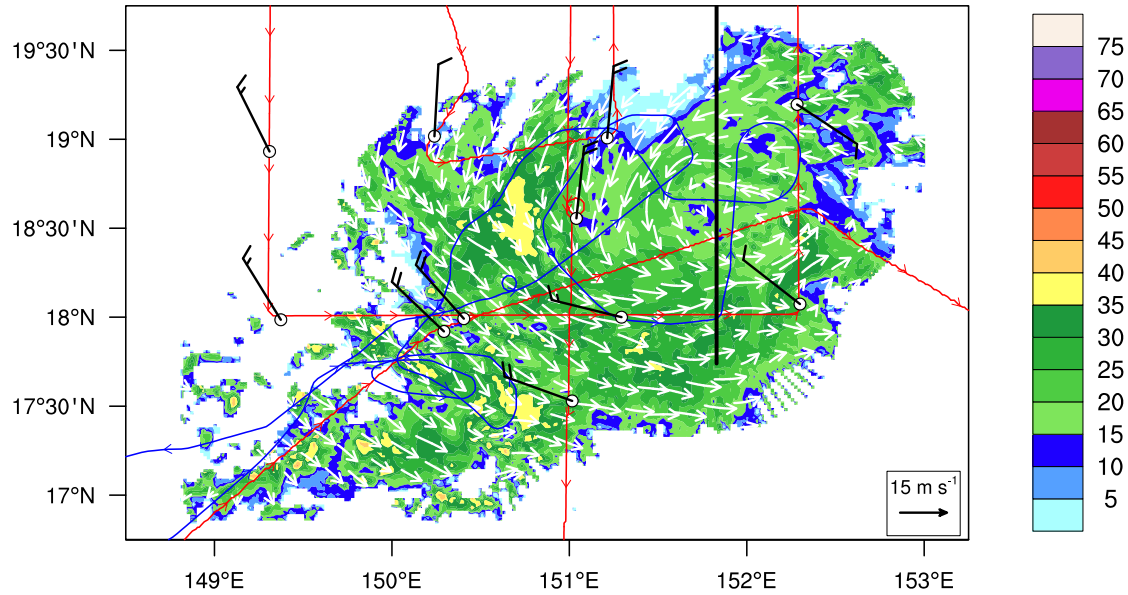


Figure 15: ELDORA reflectivity (dBZ, shading) at 5-km height from the P-3 flight 0225W early on 28 August. The white horizontal wind vectors (m s^{-1} , with 15 m s^{-1} reference vector indicated at top right) correspond to the wind field at 5-km height derived using the SAMURAI analysis technique with 2-km grid spacing. The WC-130J track for flight 0325W is in red and the P-3 track for flight 0225W is in blue. Black wind barbs correspond to dropwindsonde winds corrected for storm motion (1 full barb = 10 kt). The solid black line denotes the location of the cross-section in Fig. 14.

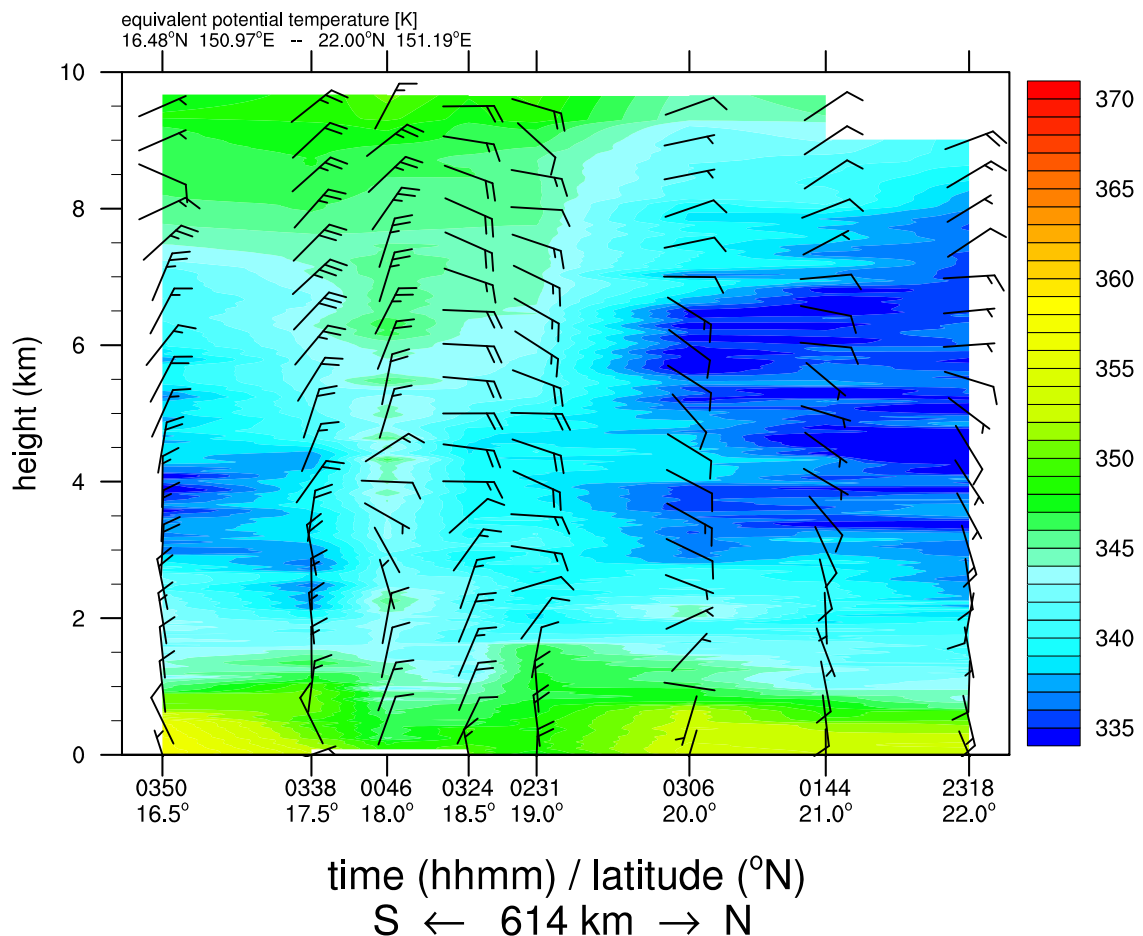


Figure 16: South-to-north vertical cross section of equivalent potential temperature (K) constructed using dropwindsonde data (red-filled circles in Fig. 11) collected during the second WC-130J flight (0325W). Wind barbs depict the dropwindsonde horizontal wind (1 full barb = 10 kt) and have been oriented to match the cross section such that wind barbs pointing from right to left correspond with northerly winds.

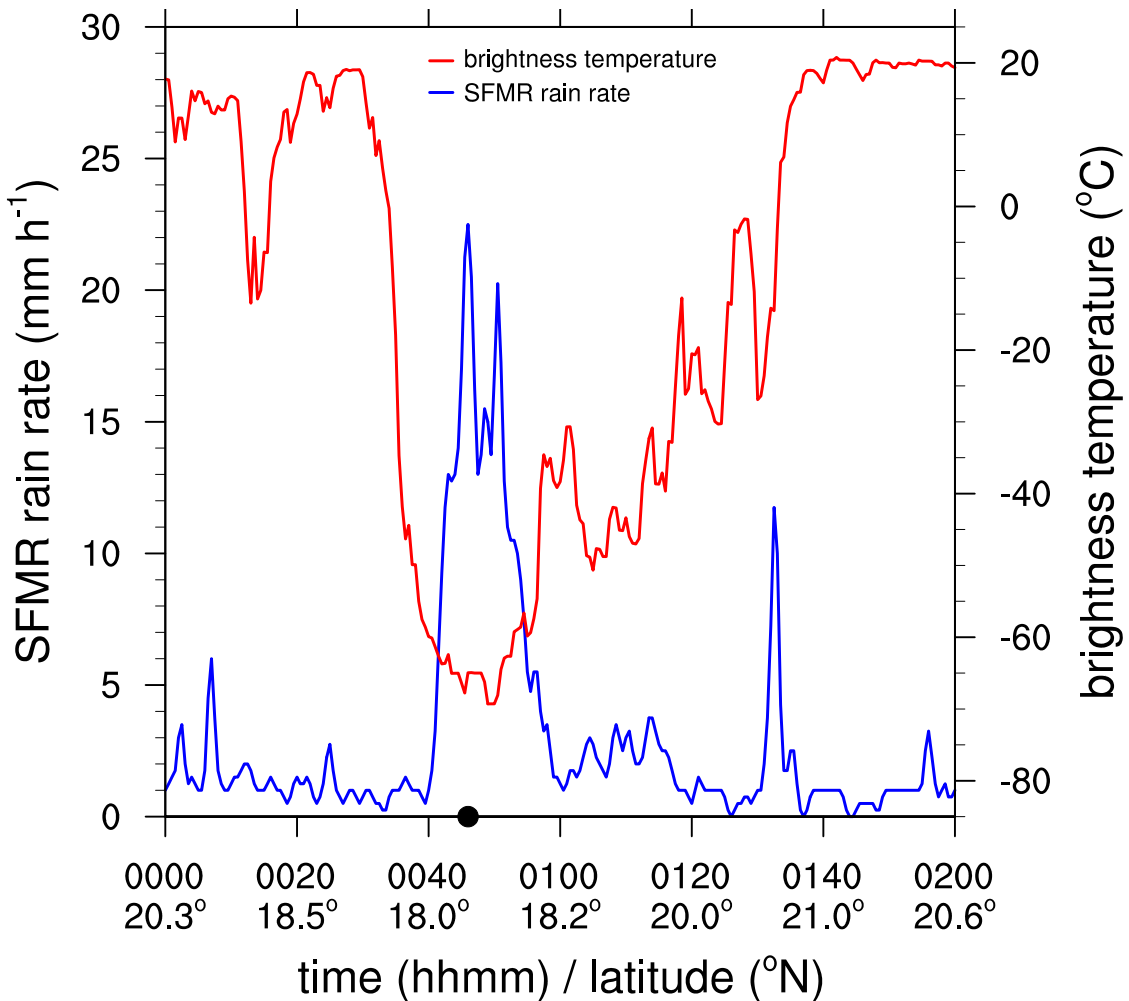


Figure 17: SFMR rain rate (mm h^{-1} , blue line and left ordinate) and MTSAT IR brightness temperatures ($^{\circ}\text{C}$, red line and right ordinate) interpolated spatially and temporally to the flight track during the second WC-130J flight (0325W) from 0000 UTC – 0200 UTC 28 August. Abscissa axis labels correspond to UTC time. Black dashed line in Fig. 11 denotes the location along the flight track corresponding to this time interval. The black circle along the abscissa indicates the time of the 0046 UTC dropwindsonde in Fig. 16.

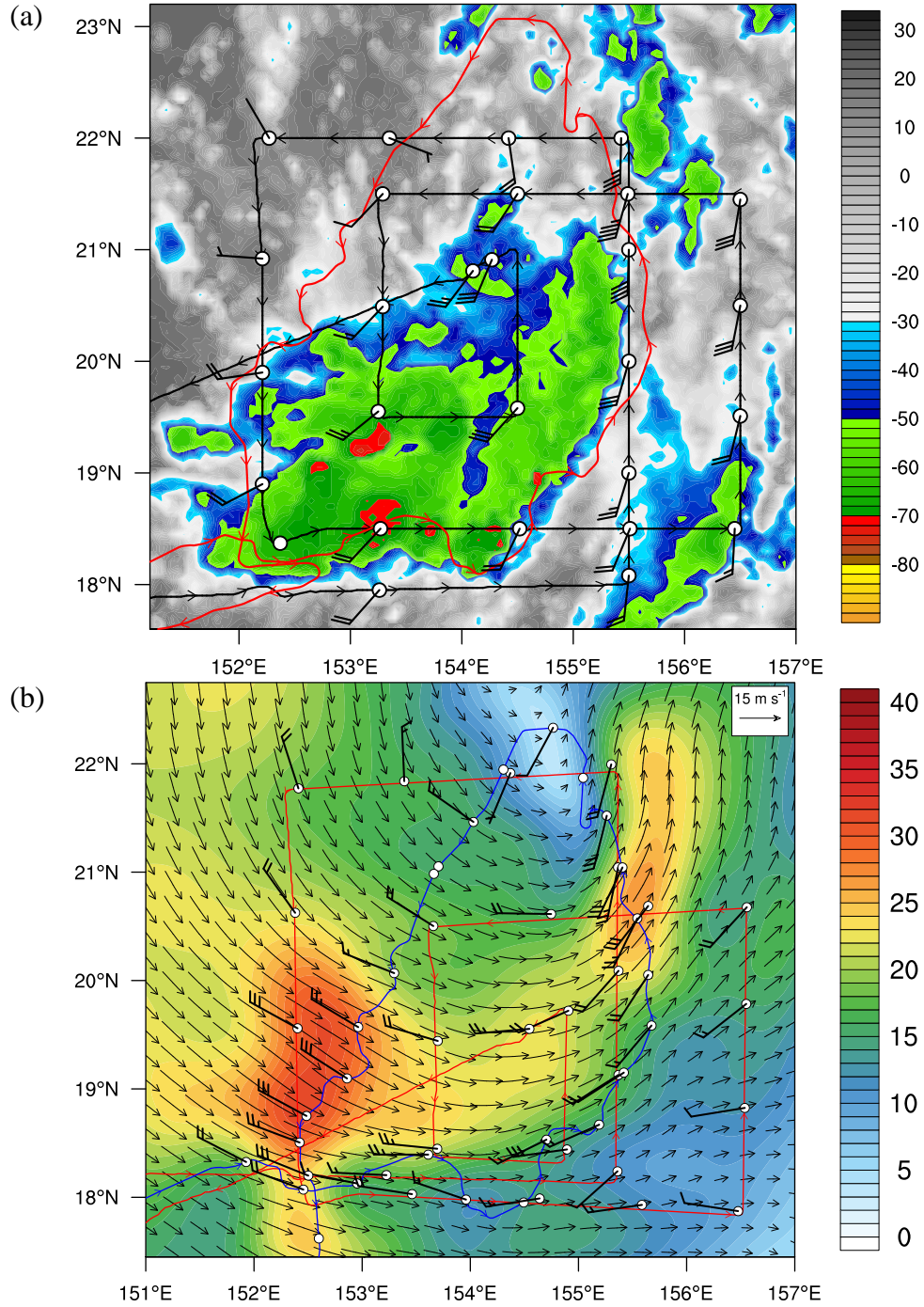


Figure 18: MTSAT IR brightness temperature ($^{\circ}\text{C}$, shading) valid at 2345 UTC 28 August with flight tracks for the WC-130J (black line) and P-3 (red line), dropwindsonde deployment locations (white circles), and horizontal dropwindsonde winds at 1.5 km height (1 full barb = 10 kt) for IOP-3 (0425W and 0525W) in the ground-relative frame. (b) As in panel (a), except for storm-relative wind speed (kt, shading) and vectors (m s^{-1}) at 1.5 km height from the 5-km SAMURAI analysis valid at 0000 UTC 29 August. Flight tracks, dropwindsonde deployment locations, and dropwindsonde winds have been adjusted for storm motion in (b).

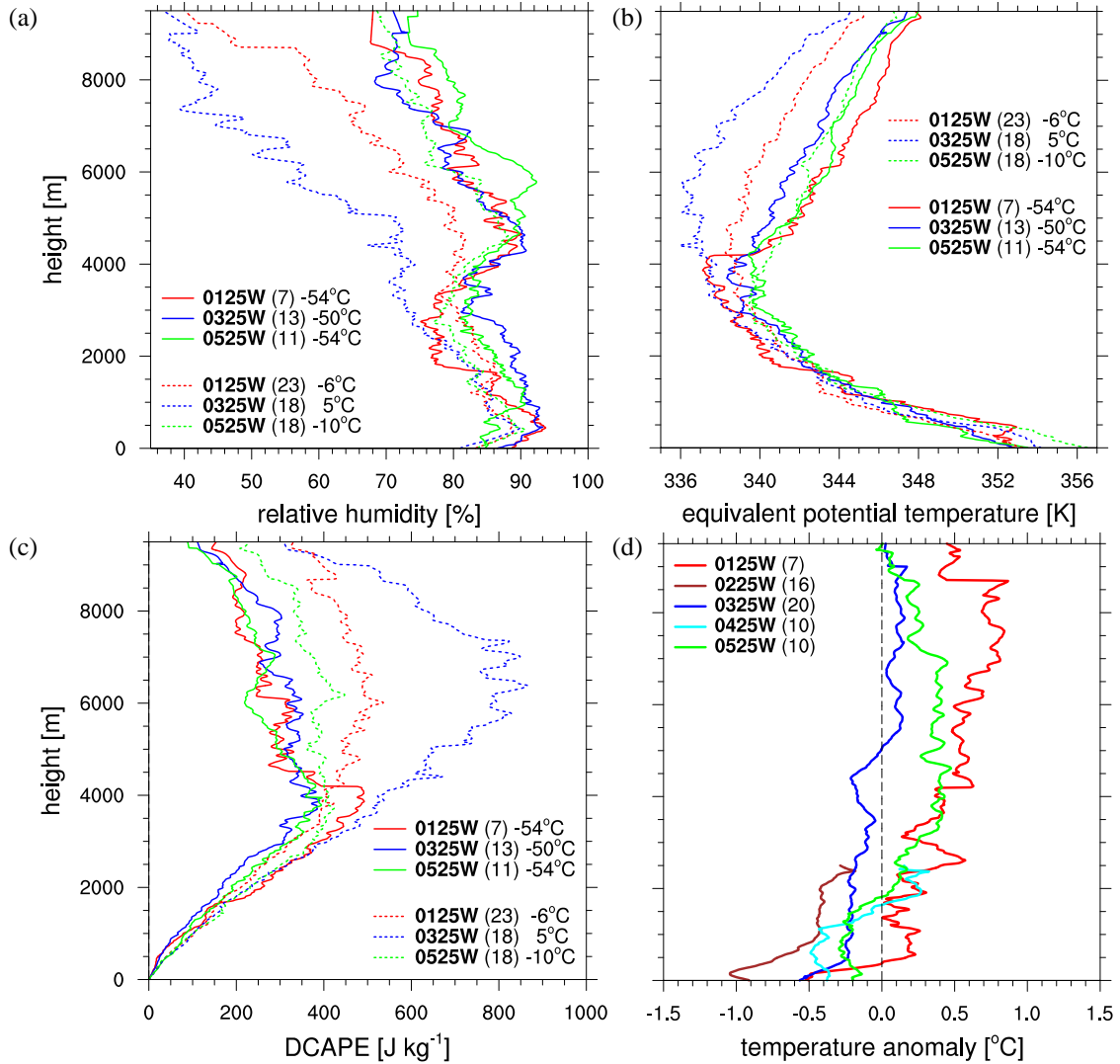


Figure 19: Vertical profiles of (a) relative humidity (%), (b) θ_e (K), and (c) DCAPE (J kg^{-1}) averaged for dropwindsondes for which the MTSAT IR brightness temperatures interpolated to the dropwindsonde time and location were less than -35°C (solid lines) and greater than -35°C (dashed lines) during WC-130J aircraft missions shown in inset. The average MTSAT IR brightness temperatures of dropwindsondes used to compute each average are shown in inset. (d) Vertical profiles of temperature anomaly (K) from dropwindsondes averaged within 250 km of the analyzed ECMWF 850 hPa circulation center during aircraft missions shown in inset. Each mean profile used to compute the average temperature anomaly was constructed from all dropwindsondes from each flight. The number of dropwindsondes used to compute each average is shown in the inset of each figure.

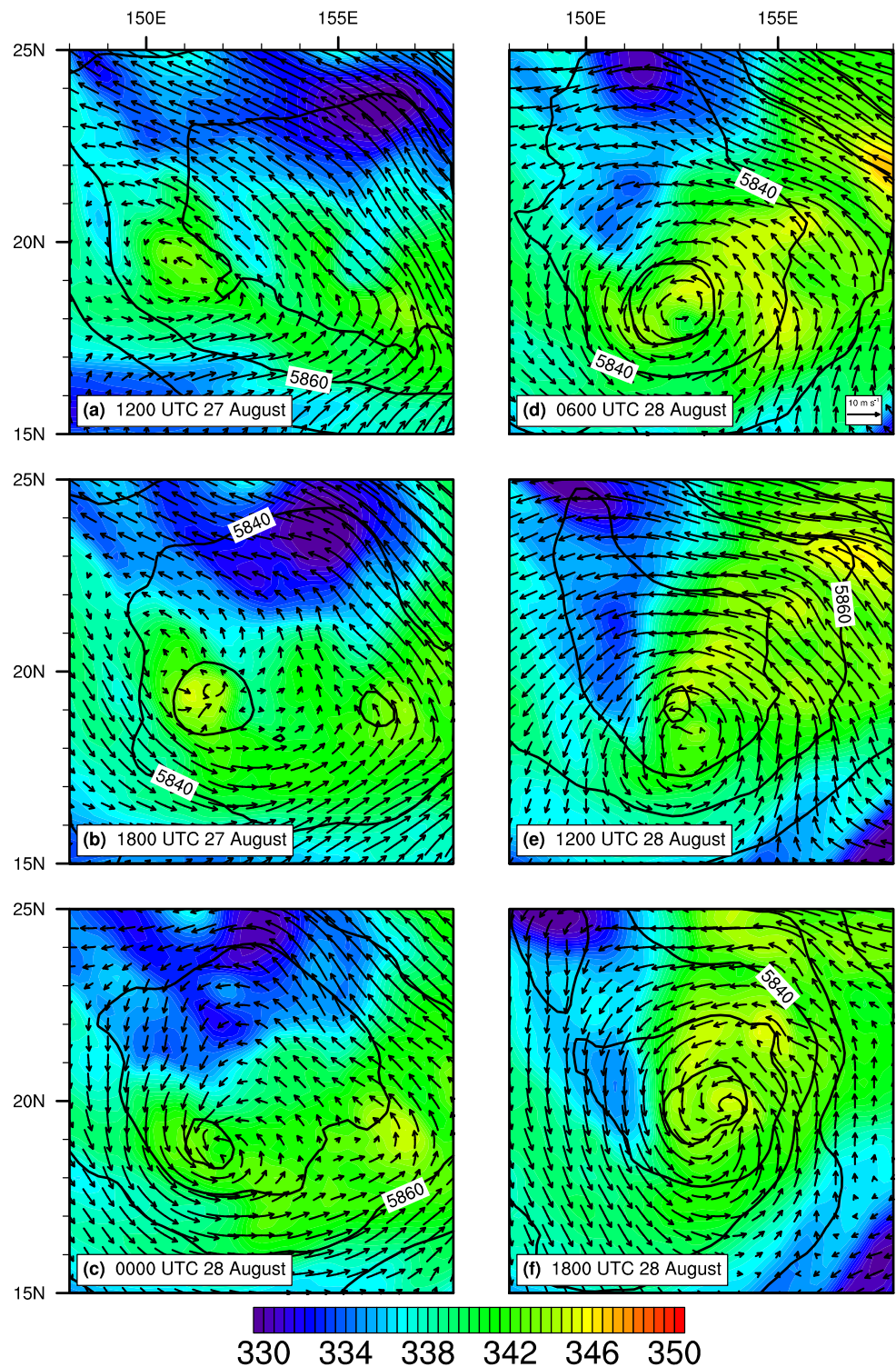


Figure 20: Equivalent potential temperature (K, shading), geopotential height (m, contours), and storm-relative wind vectors (m s^{-1} , with 10 m s^{-1} reference vector indicated at bottom right in panel-d) at 500 hPa from the ECMWF analysis at times annotated in each panel.

Tables

vertical grid spacing	T (K)	q_v (g kg ⁻¹)	ρ_a (kg m ⁻³)	$\rho u, \rho v$ (kg m ⁻² s ⁻¹)	ρw (kg m ⁻² s ⁻¹)	i, j filter	k filter
5 km	100 m	3	3	3	10	1	8
2 km	100 m	3	3	3	15	10	6

Table 1: Configurations used for the 5- and 2-km (horizontal grid spacing) SAMURAI analyses. Listed are the background error standard deviation values for temperature (T), water vapor mixing ratio (q_v), dry-air density (ρ_a), and moist-air-density-weighted wind components ($\rho u, \rho v$ and ρw). The Gaussian recursive filter lengths correspond to grid points in the horizontal (i, j) and vertical (k) directions.